

# Flow property and self-similarity in steady hydraulic jumps

Chang Lin · Shih-Chun Hsieh · I-Ju Lin ·  
Kuang-An Chang · Rajkumar V. Raikar

Received: 23 December 2011 / Revised: 28 May 2012 / Accepted: 25 August 2012 / Published online: 18 September 2012  
© Springer-Verlag 2012

**Abstract** The flow structure in a steady hydraulic jump in both the non-aerated and aerated regions was measured using the image-based particle image velocimetry and bubble image velocimetry techniques, respectively. Three highly aerated steady jumps with Froude numbers varying from 4.51 to 5.35 were tested, and a weak jump with a Froude number of 2.43 was generated for comparison. Mean velocities and turbulence statistics were obtained by ensemble averaging the repeated velocity measurements. Based on the mean velocities, the flow structure in the steady jumps was classified into four regions to distinguish their distinct flow behaviors; they are the potential core region, the boundary layer region, the mixing layer region, and the recirculation region. The flow structure in the weak jump features only three regions without the recirculation region. In addition, spatial variations of mean velocities, turbulence intensity, and Reynolds stresses were also presented. It was observed that the maximum horizontal bubble velocity and maximum horizontal water velocity occur at the same location in the overlapping regions of potential core and mixing layer. The ratio between the maximum horizontal bubble velocity and maximum horizontal water velocity is between 0.6 and 0.8, depending on

the Froude number. Examining the mean horizontal bubble velocities in the mixing layer, a similarity profile was revealed with representative mixing layer thickness as the characteristic length scale and the difference between the maximum positive and maximum negative velocities as the characteristic velocity scale. It was also found that the mean horizontal water velocities in the near-wall region are self-similar and behave like a wall jet. Further analyzing autocorrelation functions and energy spectra of the water and bubble velocity fluctuations found that the energy spectra in the water region follow the  $-5/3$  slope, whereas the spectra in the bubble region follow a  $-2/5$  slope. In addition, the integral length scale of bubbles is one order of magnitude shorter than that of water.

## List of symbols

$b$	Half-width of mixing layer for bubble velocity (L)
$b_w$	Half-width of wall jet for water velocity (L)
$C_i$	Regression coefficients, $i = 0-5$
$F_r$	Approaching inflow Froude number, $u_1/\sqrt{gy_1}$
$F_B$	Froude number determined by Belanger equation, $y_2/y_1 = 0.5(-1 + \sqrt{1 + 8F_B^2})$
$g$	Gravitational acceleration ( $LT^{-2}$ )
$I$	In-plane (equivalent) turbulence intensity, $\sqrt{u'^2 + v'^2}/u_1$
$q$	Unit-width discharge ( $L^2T$ )
$Re$	Reynolds number, $u_1 y_1/\nu$
$r$	Ratio between maximum bubble velocity and maximum water velocity
$t$	Time (T)
$U_{rms}$	Horizontal turbulence level, $\sqrt{u'^2}/u_1$
$u$	Mean horizontal velocity ( $LT^{-1}$ )
$u_1$	Average approaching velocity ( $LT^{-1}$ )

C. Lin · S.-C. Hsieh · I.-J. Lin  
Department of Civil Engineering,  
National Chung Hsing University, Taichung 402, Taiwan

K.-A. Chang (✉)  
Zachry Department of Civil Engineering,  
Texas A&M University, College Station, TX 77843, USA  
e-mail: kchang@tamu.edu

R. V. Raikar  
Department of Civil Engineering, K.L.E.S. College  
of Engineering and Technology, Belgaum 590008, India

$u_{\max}$	Maximum positive horizontal velocity ( $LT^{-1}$ )
$u_{\min}$	Maximum negative horizontal velocity ( $LT^{-1}$ )
$u'$	Horizontal velocity fluctuations ( $LT^{-1}$ )
$V_{\text{rms}}$	Vertical turbulence level, $\sqrt{v'^2}/u_1$
$v$	Mean vertical velocity ( $LT^{-1}$ )
$v'$	Vertical velocity fluctuations ( $LT^{-1}$ )
$X$	Horizontal distance from the sluice gate (L)
$\tilde{X}$	Horizontal distance from air bubble release (L)
$x$	Horizontal distance from the toe of jump (L)
$Y$	Vertical distance from the flume bed (L)
$y$	Vertical distance from the flume bed (L)
$y_1$	Pre-jump depth (L)
$y_2$	Post-jump depth (L)
$y_{\max}$	Vertical position of $u_{\max}$ for water (L)
$y_{u_{\max}}$	Vertical position of $u_{\max}$ for bubbles (L)
$y_{u_{\min}}$	Vertical position of $u_{\min}$ for bubbles (L)
$\Lambda$	(Equivalent) Reynolds stresses, $-\overline{u'v'}/u_1^2$
$\rho$	Mass density ( $ML^{-3}$ )
$\nu$	Kinematic viscosity of water ( $L^2T^{-1}$ )

## 1 Introduction

Hydraulic jumps are a natural flow phenomenon observed in rivers or downstream of hydraulic structures such as sluice gates and spillways. Based on the approaching inflow Froude number ( $F_r$ ), the jumps are classified into five types: undular jumps for  $F_r = 1.0$ – $1.7$ , weak jumps for  $F_r = 1.7$ – $2.5$ , oscillating jumps for  $F_r = 2.5$ – $4.5$ , steady jumps for  $F_r = 4.5$ – $9.0$ , and strong jumps for  $F_r > 9.0$  (Chow 1973). Hydraulic jumps have been studied for decades due to its practical importance as energy dissipator.

Although the earliest description of hydraulic jumps can be traced back to Leonardo Da Vinci in the sixteenth century (Rouse and Ince 1957), the first experimental results were published in 1820 by Bidone, who figured the ratio of sequent depths and length of jumps (Hager 1992). Existing studies of the jumps can be broadly classified into two categories: earlier studies of external flow geometry and recent studies of internal flow structure. Among early flow geometry studies, Bakhmeteff and Matzke (1935) measured the water surface of hydraulic jumps using a point gauge. Rajaratnam and Subramanya (1968) collected surface profile data from early researchers and came up with a general dimensionless free surface profile for hydraulic jumps in rectangular channels with a Froude number greater than 4. Leutheusser and Kartha (1972) studied the effects of inflow condition on hydraulic jumps and developed theoretical results on the sequent depth and length of hydraulic jumps. Mehrotra (1976) developed an

equation to predict the length of hydraulic jumps using data collected by Bakhmeteff and Matzke (1935) and Rouse et al. (1958).

More recently, investigations on internal flow structure have been focused on the velocity field, turbulent characteristics, and void fraction in the jumps. As far as the authors know, Rouse et al. (1958) performed the first detailed velocity measurements of hydraulic jumps using hot-wire anemometry. Their experiments were carried out in a wind tunnel with a fixed rigid surface boundary in the shape of a hydraulic jump. The flow structure may be quite different between the rigid surface jump and a free surface jump. Rajaratnam (1965) conducted velocity measurements using a Pitot tube in a hydraulic jump. He concluded that the velocity distribution in a hydraulic jump is similar to that in a typical wall jet. Leutheusser and Kartha (1972) measured the mean velocity using a Pitot-static tube and boundary shear stress using a Preston tube. More recently, Liu et al. (2004) used acoustic Doppler velocimetry to measure velocity, turbulence intensity, and Reynolds stresses in hydraulic jumps with  $F_r$  ranging from 2.0 to 3.2. They found that the turbulence intensity and Reynolds stresses have some degree of similarity; they both decrease rapidly with the increase of longitudinal distance from the toe of the jumps.

In the last two decades, non-intrusive optics-based techniques such as laser Doppler velocimetry (LDV) and particle image velocimetry (PIV) were employed in the studies of hydraulic jumps. Long et al. (1990) used LDV to measure the mean velocity, turbulent shear stresses, and turbulence intensity for a submerged hydraulic jump. Svendsen et al. (2000) used LDV to study turbulent characteristics in a weak turbulent jump without aeration. Hornung et al. (1995) used a control-volume analysis with the flow field measured using PIV to study a traveling hydraulic jump with a strong shear layer developed at the toe of the roller. Recently, Lennon and Hill (2006) used PIV to measure the mean and turbulent velocities and demonstrated the flow structure of hydraulic jumps with  $F_r$  varying from 1.4 to 3.0. In their study, strong scattering of laser light by the entrained air bubbles seriously impaired their measurements in the highly aerated roller region. More recently, using PIV Misra et al. (2008) presented the mean and turbulent flow structures of a weak hydraulic jump. Their study mainly focused on the process of turbulence generation in spilling breakers in surf zone.

Studies in the aerated region of hydraulic jumps have been mostly focused on the air entrainment process and quantity of entrained air bubbles. Resch et al. (1974) investigated the distributions of void ratio and bubble size in a hydraulic jump using hot-film anemometry. Their results show that a jump with a fully developed inflow retains its aerated region longer than its undeveloped

counterpart. Hoyt and Sellin (1989) used photographs and visual observation to conclude qualitatively that the flow field of a hydraulic jump is similar to that of a turbulent mixing layer. Mossa and Tolve (1998) employed a flow visualization technique to demonstrate the flow structure of a hydraulic jump and determine the position of maximum air concentration. Chanson and Brattberg (2000) studied the air–water flow properties in the shear region of hydraulic jumps with partially developed inflow conditions using dual-tip conductivity probes. Their results show that the void-fraction distribution follows the solution of diffusion equation, and the velocity profiles have a similar profile as a wall jet. Murzyn et al. (2005) examined the bubble characteristics using an optical probe and compared the results with the measurements of Chanson and Brattberg (2000). They found that the profile of void fraction is in accordance with the Gaussian distribution in the lower part of the jump, while the profile is in agreement with the error function in the upper part of the jump. Chanson (2007) reviewed the recent advances in hydraulic jumps, including the non-breaking undular hydraulic jump, positive surge and tidal bore, and air bubble entrainment. More recently, Chanson (2011) reported that, at large approaching Froude numbers ( $F_r = 3.58\text{--}12.43$ ), the strong air entrainment rate and depth-averaged void-fraction data feature a rapid de-aeration of the jump roller, and the rate of detrainment is comparatively smaller at larger Froude numbers.

The aforementioned studies facilitated the state of knowledge on hydraulic jumps, particularly for the internal flow structure. Nevertheless, all measurements of the internal flow structure in hydraulic jumps were either done outside the aerated region (or outside the roller region) or restricted to the submerged or weak hydraulic jumps with a low Froude number and thus low air entrainment. This is mainly due to the limitation of the existing measuring techniques. In the aerated region, only the characteristics of air bubble entrainment, such as void fraction and size distribution, were better understood, whereas the knowledge in the flow structures of velocity and turbulence is still quite rudimentary.

Recently, Ryu et al. (2005) developed a new technique called bubble image velocimetry (BIV) that combines the PIV technique and the shadowgraphy method for velocity measurements in aerated flows by correlating the texture of air–water interfaces in images. Ryu et al. (2007), Ryu and Chang (2008), and Chang et al. (2011) later demonstrated feasibility of the technique in the measurement of overtopping green water flows on laboratory structures caused by breaking wave impingement. By employing the BIV and PIV techniques, Lin et al. (2008) also successfully measured the velocity fields inside and outside the aerated region of a periodic oscillatory channel flow over a vertical drop pool.

The objective of the present study is to investigate the flow structure in the aerated region of steady hydraulic jumps using BIV, and the flow structure outside the aerated region using PIV. The mean flow and turbulence statistics were obtained by ensemble averaging a large number of repeated instantaneous velocity measurements. Flow classifications and similarity analysis were performed using the measured data.

## 2 Experimental setup

Laboratory experiments were performed in a recirculating flume located in the Civil Engineering Department at National Chung Hsing University. The flume test section, located at 3.0 m from the inlet of the flume, is glass walled and glass bottomed for optical access. It is 3.05 m long, 0.50 m wide, and 0.54 m high, as shown in Fig. 1a. The approach section of the flume consists of three layers of perforated steel plates, one honeycomb structure, four meshes of different openings, and a contraction section arranged sequentially to remove large-scale flow irregularities and provide a smooth inlet flow. The flow regulation was done through a control unit that features a feedback circuit and a butterfly valve. A sluice gate made of an acrylic plate of 20 mm in thickness with a streamlined edge was installed in front of the test section to produce desired supercritical flows of depth  $y_1$ . The beginning (toe) of the jump was approximately 0.70 m from the sluice gate.

Three steady hydraulic jumps having approaching inflow Froude numbers,  $F_r$ , of 4.51, 5.00, and 5.35 were generated, as well as a weak jump with a low Froude number of 2.43 was tested for comparison. The Froude number is defined as  $F_r = u_1/\sqrt{gy_1}$  in which  $u_1$  is the depth-averaged approaching inflow velocity obtained by PIV measurements at the approach section right before the jump where the water depth is  $y_1$  and  $g$  is the gravitational acceleration. Table 1 lists detailed experimental conditions of the jumps with  $y_2$  being the post jump depth,  $F_B$  denoting the Froude number determined using the Belanger equation  $y_2/y_1 = 0.5\left(-1 + \sqrt{1 + 8F_B^2}\right)$ , and  $Re = u_1y_1/\nu$  representing the Reynolds number. The values of  $F_r$  and  $F_B$  are nearly identical in the table, confirming satisfactory jump conditions in the experiments.

A PIV system was used to measure two-dimensional velocity fields of water in the non-aerated region of the hydraulic jumps. A 7-W continuous-wave argon-ion laser was used as the light source in the PIV system. The laser beam passed through a glass cylinder of 5.7 mm in diameter; it was then reflected and spread into a 1.5-mm-thick fan-shaped light sheet as illustrated in Fig. 1b. Aluminum

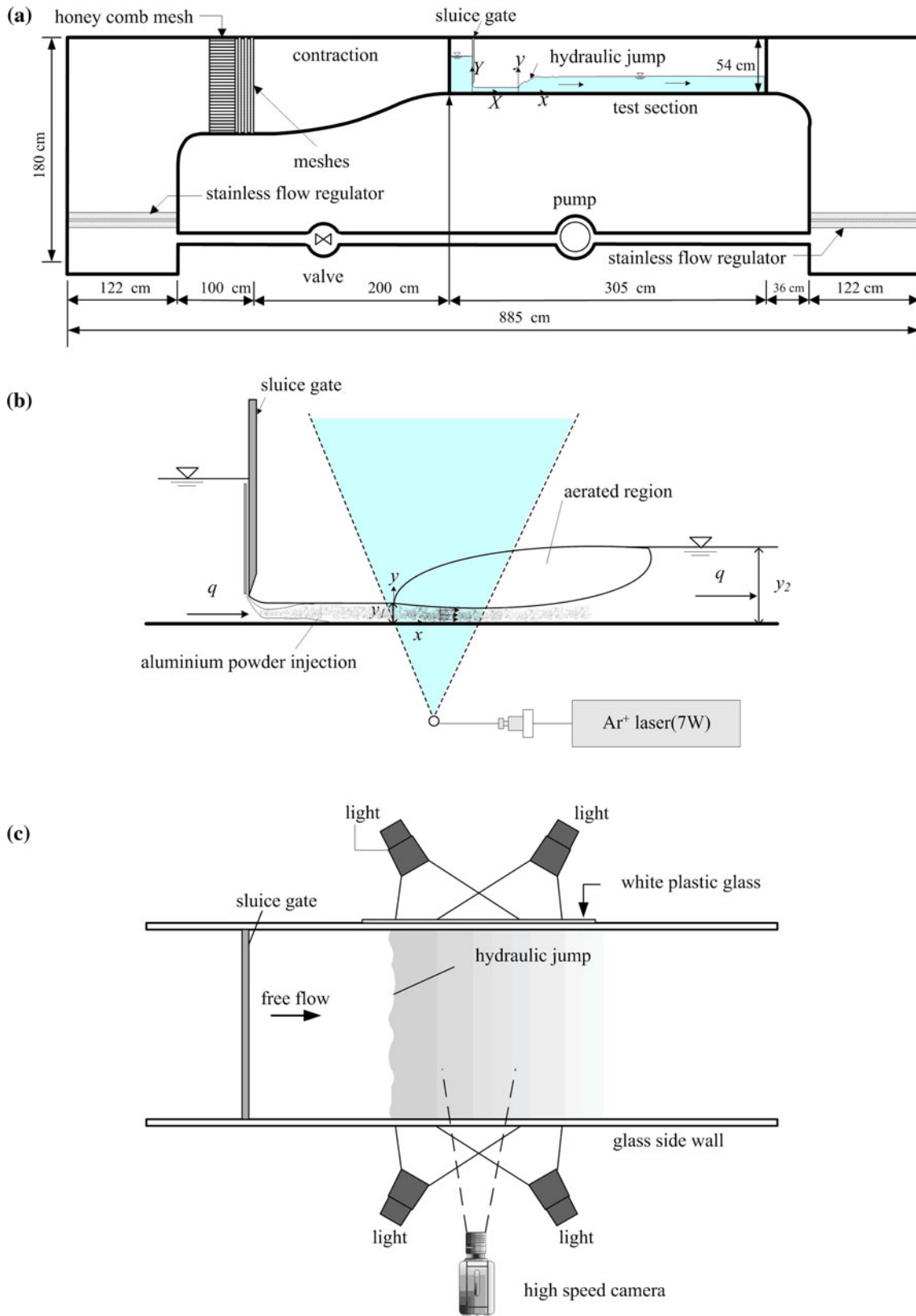


**Fig. 1** a Schematic diagram of water flume, b experimental setup of PIV system, and c experimental setup of BIV system

**Table 1** Experimental conditions of a weak jump and three steady jumps

Case	$F_r$	$y_1$ (cm)	$y_2$ (cm)	$u_1$ (cm/s)	$F_B$	$Re$
1	2.43	1.92	5.7	106.3	2.45	$8.5 \times 10^5$
2	4.51	1.95	11.5	197.3	4.51	$1.4 \times 10^6$
3	5.00	2.00	13.2	221.6	5.00	$1.6 \times 10^6$
4	5.35	1.95	13.8	233.7	5.34	$1.6 \times 10^6$

particles with a 10- $\mu\text{m}$  mean diameter and 2.7 specific gravity were used as seeding in the experiments. A high-speed digital camera with a  $1,024 \times 1,024$  pixel resolution, 10-bit dynamic range, and 1,200-Hz maximum framing rate was used to capture the particle laden images. The camera was fitted with a 60-mm focal lens and operated at 1,000 frames per second throughout the experiments. Velocity fields of the non-aerated region were determined by cross-correlation analysis. A multi-grid interrogation process starting at  $64 \times 16$  pixels and ending at  $16 \times 4$  pixels ( $0.73 \times 0.18$  mm) with 50 % overlap between adjacent sub-windows was used in the process. Due to strong light reflection from the entrained air bubbles, images in the aerated region were very difficult to process using traditional PIV method.

The BIV technique developed by Ryu et al. (2005) was used for obtaining the velocity fields in the aerated region of the hydraulic jumps. Note that BIV works only in the region where PIV does not work well or does not work at all. Figure 1c shows the setup of the BIV system. Four 600-W light bulbs were used to illuminate the flow with two bulbs on each side of the flume. The center of focal plane in the BIV measurements is 10.0 cm behind the frontal glass tank wall. A thin translucent plastic sheet was attached to the rear glass wall of the flume to create bubble shadows in the BIV images. Note that no laser is needed in BIV. The high-speed camera and image processing software used in PIV were also employed in BIV image acquisition and analysis. A similar multi-grid interrogation process starting at  $32 \times 32$  pixels and ending at  $16 \times 8$  pixels ( $2.47 \times 1.24$  mm) with 50 % overlap between adjacent sub-windows was used in the process. The details of the BIV technique can be found in Ryu et al. (2005). A LDV system was also used for validation purpose. The details of the LDV system can be found in Lin et al. (2007).

Figure 2 illustrates the coordinate systems and various fields of view (FOVs) employed in the PIV and BIV measurements in the experiments. The origin of the coordinate system ( $x, y$ ) is located at the bottom of the flume and the toe of the hydraulic jump with  $x$  in the horizontal streamwise direction and  $y$  in the vertical upward direction. Seven FOVs (termed FOVP1 to FOVP7) were used for the PIV measurements and five FOVs (termed FOVB1 to

FOVB5) for the BIV measurements as shown in the figure. The FOVPs cover the region from  $x < 0$  to  $x = 26$  cm ( $x/y_1 = 14.1$ ), while the FOVBs cover the region from  $x < 0$  to  $x = 40$  cm ( $x/y_1 = 21.7$ ). The FOVs have certain overlap areas between adjacent FOVs to ensure continuous coverage in space. The size of the FOVPs is  $75.0$  mm  $\times$   $37.5$  mm, while the size of the FOVBs is  $170.0$  mm  $\times$   $85.0$  mm. The time interval between the recorded images is 1.0 ms for all the PIV and BIV measurements because of the use of 1,000-Hz camera framing rate. Mean velocities were calculated by ensemble averaging 16,000–19,000 instantaneous velocity fields of repeated measurements in both the PIV and BIV measurements. The final results are a mosaic of measurements from the 12 FOVs with 16,000–19,000 repeated measurements in each FOV.

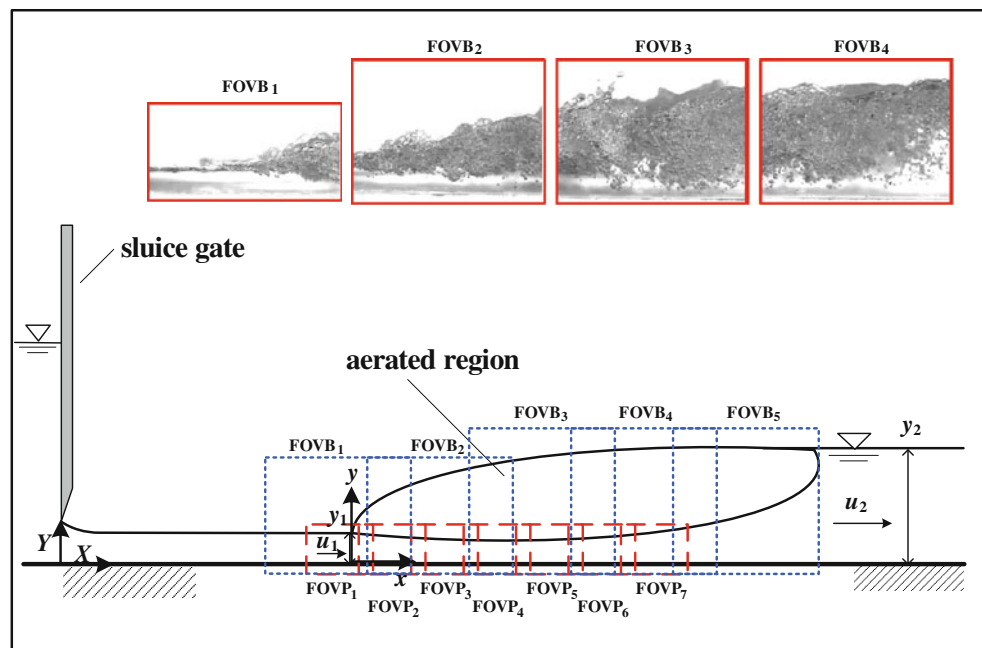
Error in the BIV measurements mainly consists of two sources. One is the installation-related error due to a limited depth of field (DOF), and the other is the pixel-resolution-related error in BIV image processing for displacement determination. The DOF was calculated as  $D = 6.8$  cm based on camera set-up and property. With the camera being located at a distance of  $L_d = 1.5$  m from the focal plane, the relative error  $[=D/(2L_d)]$  reported by Ryu et al. (2005) due to the limited DOF in the measurements is about 2.3 %. The second error stemming from displacement determination can be estimated as follows. The most prominent velocity gradient in the mixing layer in the bubble velocity field is about 1.5 m/s/0.01 m (see Fig. 9 for the  $x/y_1 = 1.33$  profile). For the framing rate of 1,000 Hz in the BIV measurements, the gradient (in terms of displacement in pixel) is equal to 0.15 pixel/pixel, so the corresponding uncertainty is about 0.3 pixel (Keane and Adrian 1992), equivalent to 2.8 % of  $u_1$ . Accordingly, the total relative error at the largest velocity gradient in the bubble velocities is approximately 5.1 %.

### 3 Validation of jump characteristics and BIV measurements

The present study focused mainly on the velocity and turbulence characteristics of steady jumps having approaching Froude number from  $F_r = 4.51$ – $5.35$ . Even though the range of Froude numbers lies in the steady jump range between  $F_r = 4.5$  and  $F_r = 9.0$  (Chow 1973), the steadiness of the jumps was checked by plotting the time history of the toe location following the procedure of Long et al. (1991). For the case of  $F_r = 4.51$ , the variation of the non-dimensional toe location  $X/y_1$  versus time  $t$  over an interval of 2.75 s is illustrated in Fig. 3. The data indicate the toe moved slightly with a standard deviation of 16 mm that is less than  $y_1$  therefore the jump is considered as



**Fig. 2** PIV and BIV FOVs, coordinate systems, and definition of variables



relatively steady. Similar conclusion was found in the other two steady jump cases.

The BIV technique was validated during its development by comparing its measurements of bubble velocities in a quasi-steady bubble plume with measurements taken using the fiber optic reflectometry technique (Chang et al. 2003) and reported in Ryu et al. (2005). In the present study, more validations were performed to ensure the feasibility of the technique applied in hydraulic jump measurements. The BIV technique was validated by comparing the mean velocity of bubbles measured using BIV with that of water measured using PIV. Since the correlation software used for velocity determination was shared between PIV and BIV in the present study, the PIV measurements were first validated by comparing the PIV measurement results with measurements taken using LDV at three cross-sections in the  $F_r = 4.51$  jump. Figure 4 shows the comparisons and good agreement.

In BIV validation, air bubbles were released one by one from a fixed location on the bottom of the flume into a fully developed nearly uniform stream flow that has an average flow velocity  $u_0$ . The flow rate was kept constant in each test with a given  $u_0$ , whereas  $u_0$  was varied 11 times with its value ranging from 7.3 to 54.1 cm/s in the tests. The velocities of bubbles were calculated using two methods: finite differencing the centroid trajectory of bubble images and BIV.

Firstly, the centroid position of a particular bubble was determined from its BIV image at each time frame; its velocity was then calculated using central differences. Figure 5a shows the centroid trajectory of a bubble in the test with  $u_0 = 54.1$  cm/s; the corresponding bubble

velocities and mean water velocities are shown in Fig. 5b. Ten bubbles were traced for each  $u_0$ , and the mean velocities were compared with the water velocities measured using PIV. Figure 5c shows the ten bubble velocities and the mean bubble velocity calculated from these 11 velocities. The mean water velocity was also plotted for comparison. The figure shows that the bubble velocity is very close to the water velocity in such uniform flow condition. The ratio of mean bubble velocity and mean water velocity is 1.03, indicating that the bubbles pretty much move with the water, at least in the uniform flow with an absence of mean shear. Similar results were found for bubbles in all other  $u_0$  cases.

Secondly, based on the same images, successive BIV images were analyzed using multi-grid interrogation process for velocity determination. Images formed by each bubble create a distinct image pattern that was used to obtain velocities through cross-correlation. Figure 5d shows superimposed velocities of a single bubble at three instants. The final bubble velocity at each instant was calculated by averaging the vectors in each bubble. The bubble velocities obtained using the two methods above were then plotted together for comparison and shown in Fig. 5e. The discrepancy is 3.3 %, indicating the BIV technique works well in measuring the bubble velocities.

#### 4 Mean flow properties

The velocity fields in the water region and aerated region of the hydraulic jump were measured separately using the PIV and BIV techniques, respectively. Figure 6a

**Fig. 3** **a** Time history of toe location for the  $F_r = 4.51$  jump. **b** Images with the toe of the jump at four consecutive instants with a 10-ms interval. The vertical line in each panel indicates the mean location of the jump

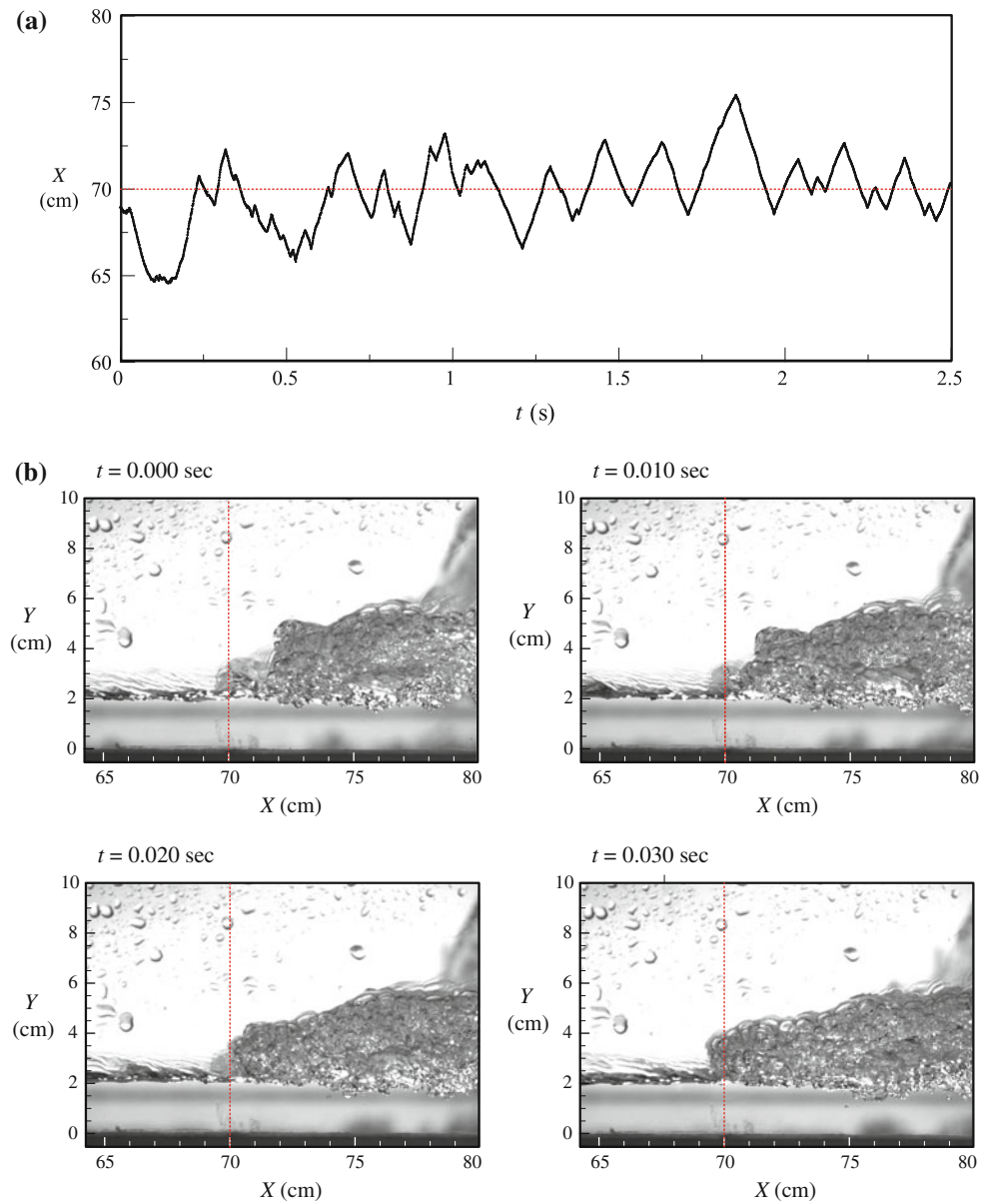


**Fig. 4** Comparisons of PIV and LDV mean water velocity measurements for the  $F_r = 4.51$  jump at  $x =$  **a**  $-5$  cm, **b**  $0$  cm, and **c**  $10$  cm

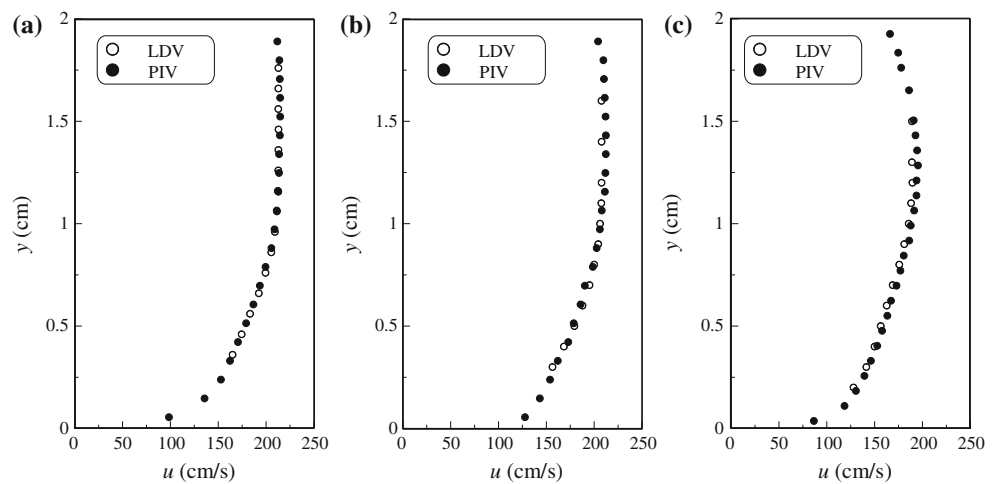
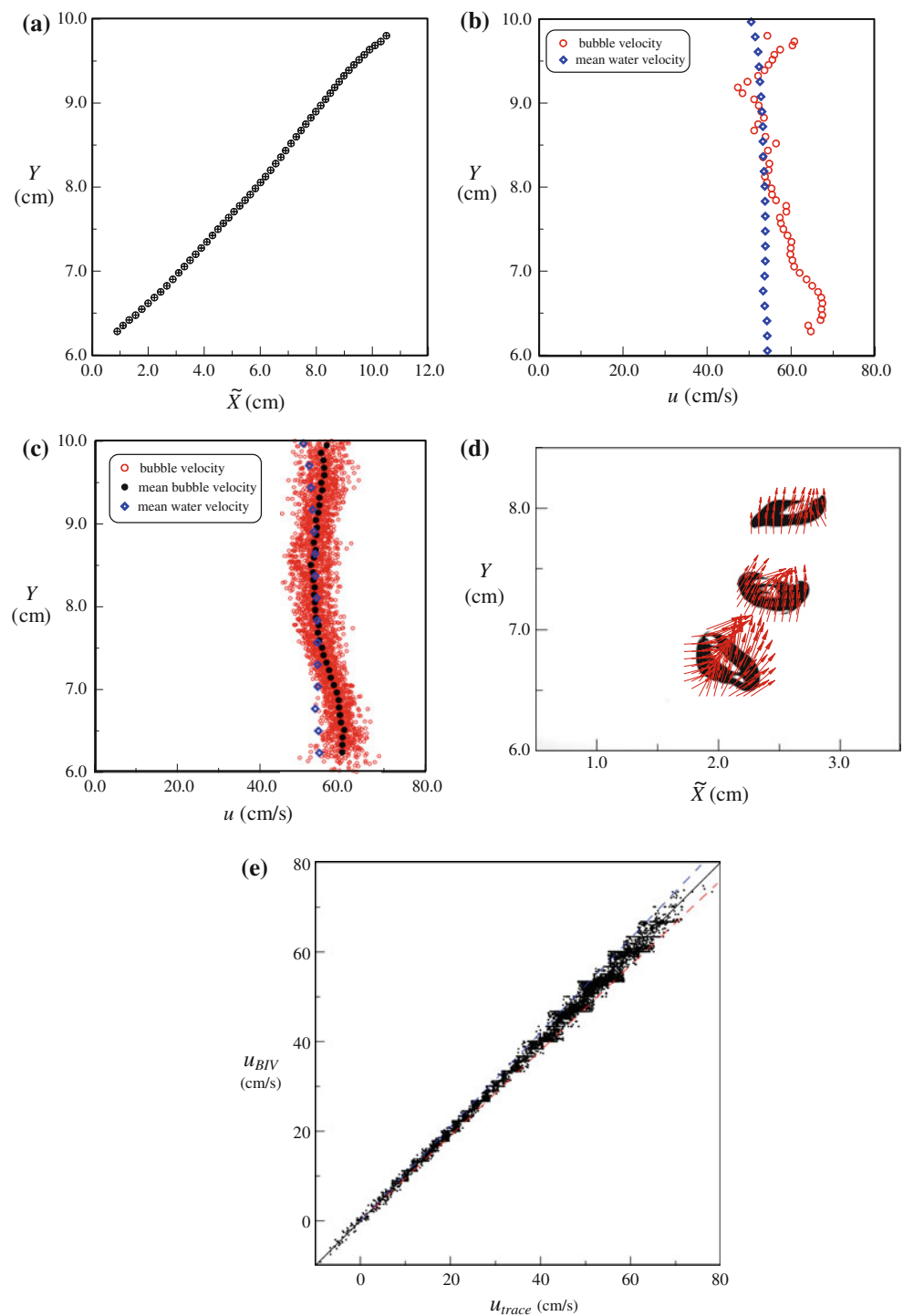


**Fig. 5** **a** Centroid trajectory of a bubble released into a uniform stream with  $u_0 = 54.1$  cm/s; **b** corresponding bubble velocities (*open circle*) and mean water velocity (*open diamond*); **c** instantaneous velocities (*open circle*) of 10 bubbles and the corresponding mean bubble velocity (*filled circle*) and mean water velocity (*open diamond*); **d** superposition of BIV velocity measurements of a bubble at three instants with a 0.027-s time interval between adjacent instants. Note that  $\tilde{X}$  is the horizontal distance from the air bubble releasing point. **e** Comparison of bubble velocities determined using BIV and centroid trajectories with  $u_0$  ranging from 7.3 to 54.1 cm/s. The two dashed lines are 5 % deviation limits



demonstrates a typical PIV image in the water region of a steady jump ( $F_r = 4.51$ ); the corresponding instantaneous water velocity field obtained using PIV is illustrated in Fig. 6b. Figure 6c demonstrates a typical BIV image in the aerated region of a steady jump. A huge number of air bubbles made it difficult to apply PIV in such a region. On the contrary, more bubbles are better for BIV since it correlates the texture of bubbles in the

images. Figure 6d shows the corresponding instantaneous bubble velocity field.

The mean velocities in the water region and in the aerated region were obtained by ensemble-averaging velocities measured using PIV and BIV as discussed above and then superimposed to form a complete two-phase velocity field. To better understand the difference between the steady jumps ( $F_r = 4.51$ –5.35) investigated in the



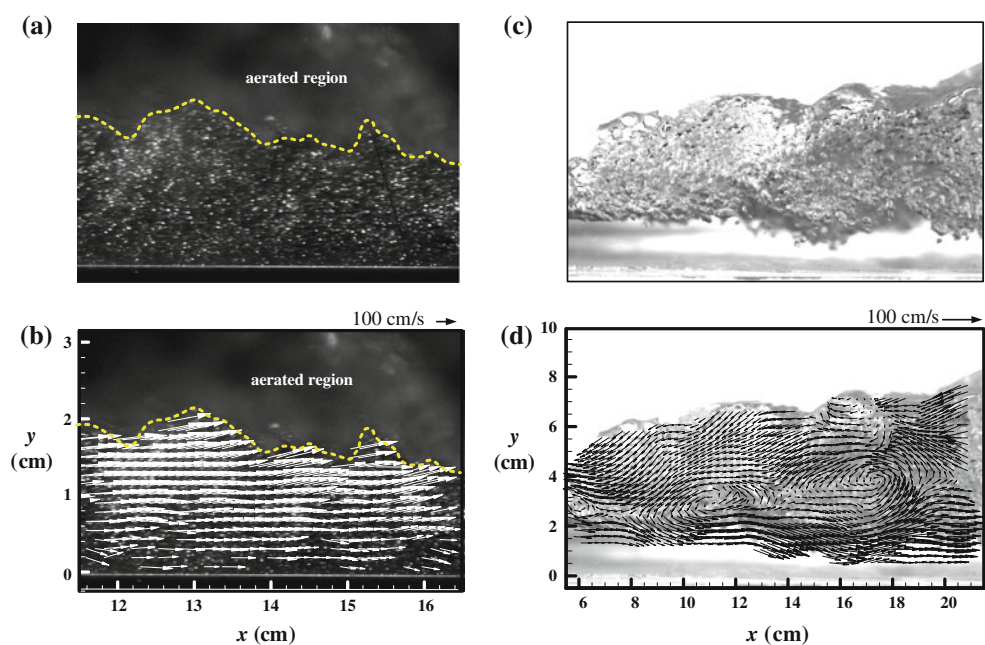
present study and weak jumps studied by others, the mean velocity field of a weak jump ( $F_r = 2.43$ ) was also measured using PIV and BIV. The mean velocity field of the weak jump is shown in Fig. 7a, while the mean velocity fields of two steady jumps ( $F_r = 4.51$  and  $5.00$ ) are shown in Fig. 7b, c. As shown in the figure, the most prominent difference between a weak jump and a steady jump is that the aerated region in a weak jump is relatively small and confined only near the free surface shortly behind the toe of the jump. In addition, there is no mean flow reversal (i.e., no recirculation region) in the weak jump, whereas a strong flow reversal can be clearly observed in the steady jumps. Note that differences among the three steady jumps tested in the present study are insignificant because of a narrow range in the Froude number.

Based on the velocity fields presented in Fig. 7a–c, it was found that flow structure in the weak jump can be classified into three distinct regions, namely a *potential core* region, a *boundary layer* region, and a *mixing layer* region as indicated in Fig. 8a. On the other hand, the flow structure in the steady jumps can be categorized as four different regions, namely a *potential core* region, a *boundary layer* region, a *mixing layer* region, and a *recirculation* region as indicated in Fig. 8b, c. The region of the incoming supercritical flow that extends about 6 times and more than 10 times the approaching water depth, respectively, is classified as the potential core by analogous to that in a turbulent jet. The length of the core depends on the Froude number of the incoming flow; the higher the Froude number, the longer the length (normalized by  $y_1$ ), at least for the four Froude numbers tested in the present

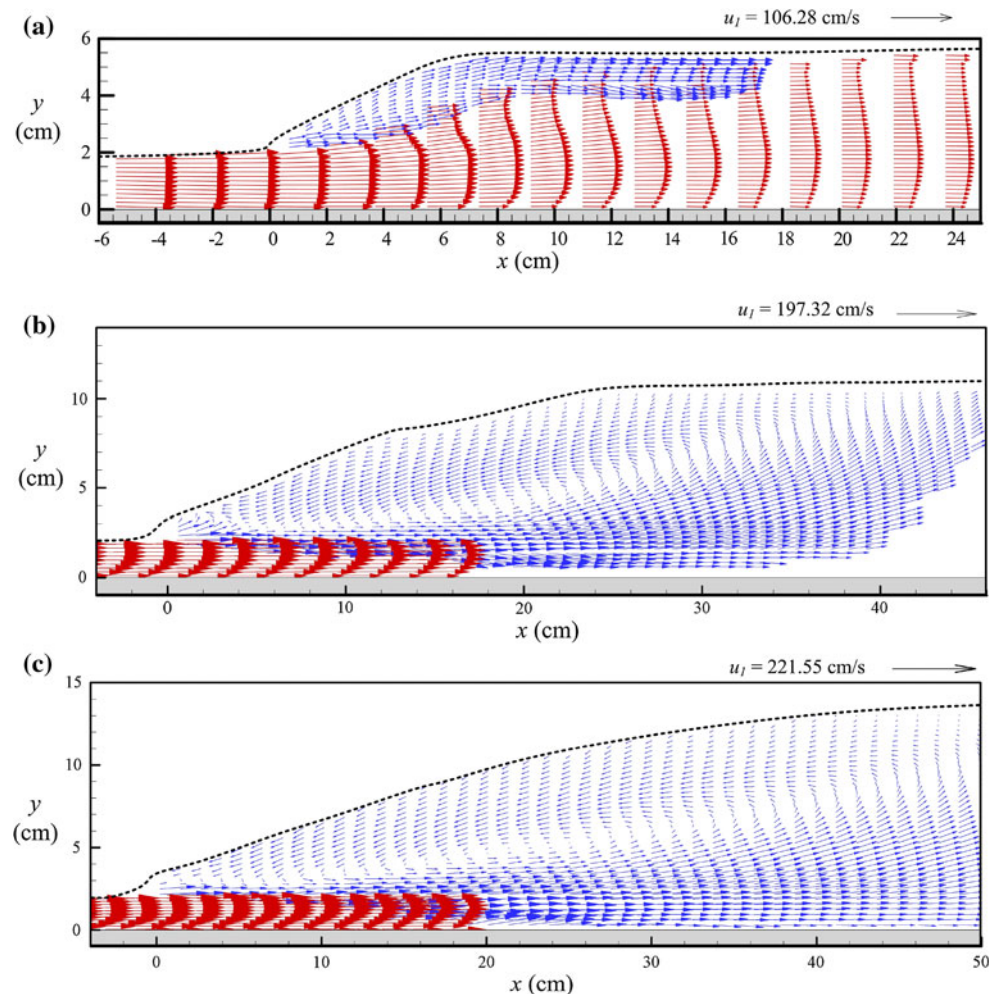
study. A thin bottom boundary layer continues to develop from the upstream. The thickness extends to the lower bound of the potential core and continues to increase until beyond the potential core region as the uniform shooting flow in the potential core diminishes. On the other hand, the mixing layer and recirculation zone develop right at the toe of the jump and above the potential core. The mixing layer seems to be bounded by the lines formed by the maximum positive and maximum negative horizontal velocities. The thickness of the mixing layer increases with the distance from the toe. Moreover, the region above the mixing layer is considered as the recirculation zone in which the flow is in the reverse direction and highly aerated. Note that for the weak jump ( $F_r = 2.43$ ) tested here, it has neither a mean flow reversal nor does it have a recirculation zone above the mixing layer. Since weak jumps have been studied by several researchers with detailed velocity measurements, the present study focuses mainly on the steady jumps that have rarely been reported with detailed velocity measurements due to hurdles caused by air bubbles.

Figure 9 shows the vertical distributions of the mean horizontal velocity  $u/u_1$  (normalized by the average approaching velocity  $u_1$ ) for the  $F_r = 4.51$  jump at 15 different cross-sections downstream from the toe. Note that at the first five cross-sections near the toe ( $x/y_1 = 1.33$ – $6.4$ ), the bubble density is relatively low with intermittent occurrence in the potential core and lower part of the mixing layer regions. As a result, mean water and bubble velocities were measured successfully by PIV and BIV (as represented by hollow circles and solid circles in the figure), respectively. However, the obtained velocities

**Fig. 6** **a** Typical PIV image of the water region of a steady jump with  $F_r = 4.51$ ; **b** corresponding instantaneous water velocity field obtained by PIV. **c** Typical BIV image of the aerated region; **d** corresponding instantaneous bubble velocity field obtained by BIV



**Fig. 7** Mean water and bubble velocity fields of **a** a weak jump with  $F_r = 2.43$ ; and **b**, **c** two steady jumps with  $F_r = 4.51$  and 5.00, respectively. *Red vectors* water velocities from PIV measurements; *blue vectors* bubble velocities from BIV measurements



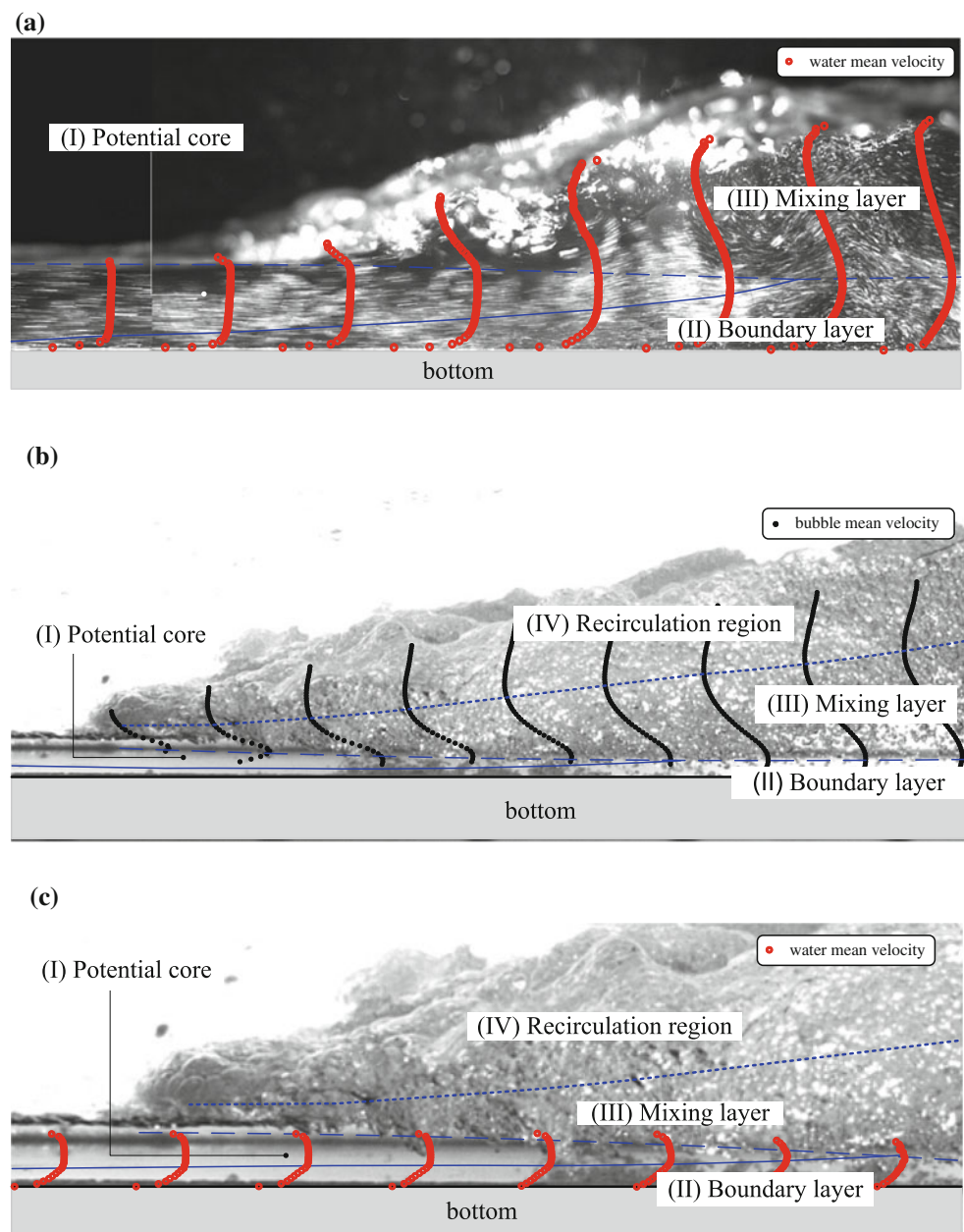
in the overlap region are not identical due to the fact that the techniques measure different velocities (water and bubbles). Unlike the nearly identical velocities between water and bubbles presented in Fig. 5 under the uniform velocity condition, velocities between water and bubbles are quite different in a shear flow. The velocity ratio and discrepancy will be presented and discussed later in Fig. 11.

In Fig. 9, it was found that the mean horizontal water velocity increases from the bottom surface in the boundary region and reaches a maximum value close to unity ( $u/u_1 = 1$ ) in the potential core region. The magnitude of mean horizontal water velocity remains nearly constant in the potential core region ( $x/y_1 = 1.33$ – $3.87$ ), somewhat similar to a turbulent jet flow. The end of the potential core is determined by not having a constant velocity distribution ( $x/y_1 = 5.13$ ). Above the potential core, the mean horizontal velocity decreases in the mixing layer. The mixing layer is characterized by the reversal of mean horizontal bubble velocity. In the lower part, the mean horizontal bubble velocity is positive; the velocity then decreases and

becomes negative toward the recirculation zone. The lower bound of the mixing layer is coincident with the maximum positive mean horizontal bubble velocity, and the upper bound of the mixing layer is coincident with the maximum value of reversed horizontal bubble velocity (maximum negative bubble velocity), as indicated by the dotted lines in Fig. 9. Furthermore, in the recirculation zone, the velocities are all negative; the negative mean horizontal bubble velocity decreases and becomes almost zero near the free surface. Similar flow patterns were also observed for other two steady jumps with Froude numbers 5.00 and 5.35.

Figure 10 shows the vertical distributions of mean vertical velocity  $v/u_1$  (normalized by the average approaching velocity  $u_1$ ) for the  $F_r = 4.51$  jump at 15 cross-sections corresponding to Fig. 9. The magnitude of the vertical velocity is one order lower than that of the horizontal velocity. It was found that in the upstream part of the potential core ( $x/y_1 < 3.87$ ), the mean vertical water velocity is negligibly small; it is the mean horizontal velocity  $u/u_1$  that predominates. Toward the end of the

**Fig. 8** Classification of flow structure into different regions separated by the *blue lines*: **a** three regions for the weak jump with  $F_r = 2.43$ ; **(b, c)** four regions for the steady jump with  $F_r = 4.51$ , along with the distributions of mean bubble velocities and mean water velocities, respectively

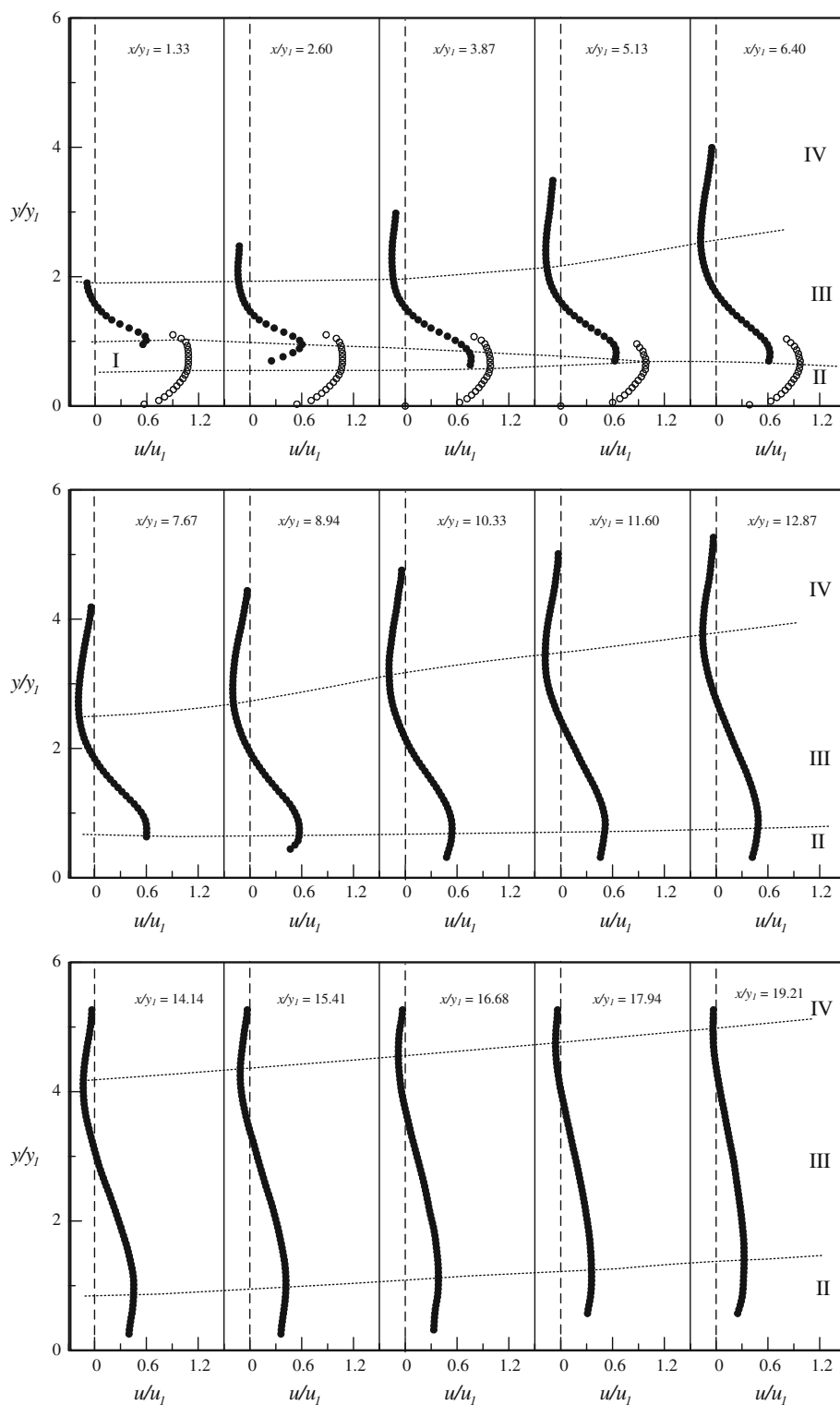


core, the mean vertical water velocity is positive, implying the flow is raised and mixed with that in the mixing layer above. On the contrary, the mean bubble velocity is negative, indicating a downward motion of air bubbles mixed with the upward movement of water in such a region. Further downstream ( $x/y_1 > 14.14$ ) near the bottom boundary, the bubble velocity is all positive and extends to the mixing layer with a maximum magnitude of about  $v/u_1 = 0.1$ . On the other hand, the sign changes from positive to negative in the most part of the mixing layer before  $x/y_1 = 15.41$ , indicating flow mixing. It is not difficult to identify the mixing layer based on the reversal of mean vertical bubble velocity from positive to negative.

Above the mixing layer, the mean vertical bubble velocity remains negative and almost constant near the free surface.

The mean horizontal velocities  $u/u_1$  measured using PIV and BIV in the aerated overlap zone in the potential core region are different, but their variation follows a similar pattern as demonstrated in Fig. 9 (from  $x/y_1 = 1.33$ – $3.87$ ). The velocities of air bubbles are much lower than that of water. The slip-velocity effect is the likely cause because of drag forces applied on the bubbles due to the large velocity gradient and buoyancy, resulting in the bubble motion to deviate from the water motion to a certain extent. Based on our observation from high-speed video images

**Fig. 9** Vertical distributions of mean horizontal velocity  $u/u_1$  at 15 different cross-sections obtained by PIV and BIV for the  $F_r = 4.51$  jump. *Open circle* water velocity by PIV measurements; *Filled circle* bubble velocity by BIV measurements. I, II, III, and IV indicate the potential core, boundary layer, mixing layer, and recirculation regions, respectively

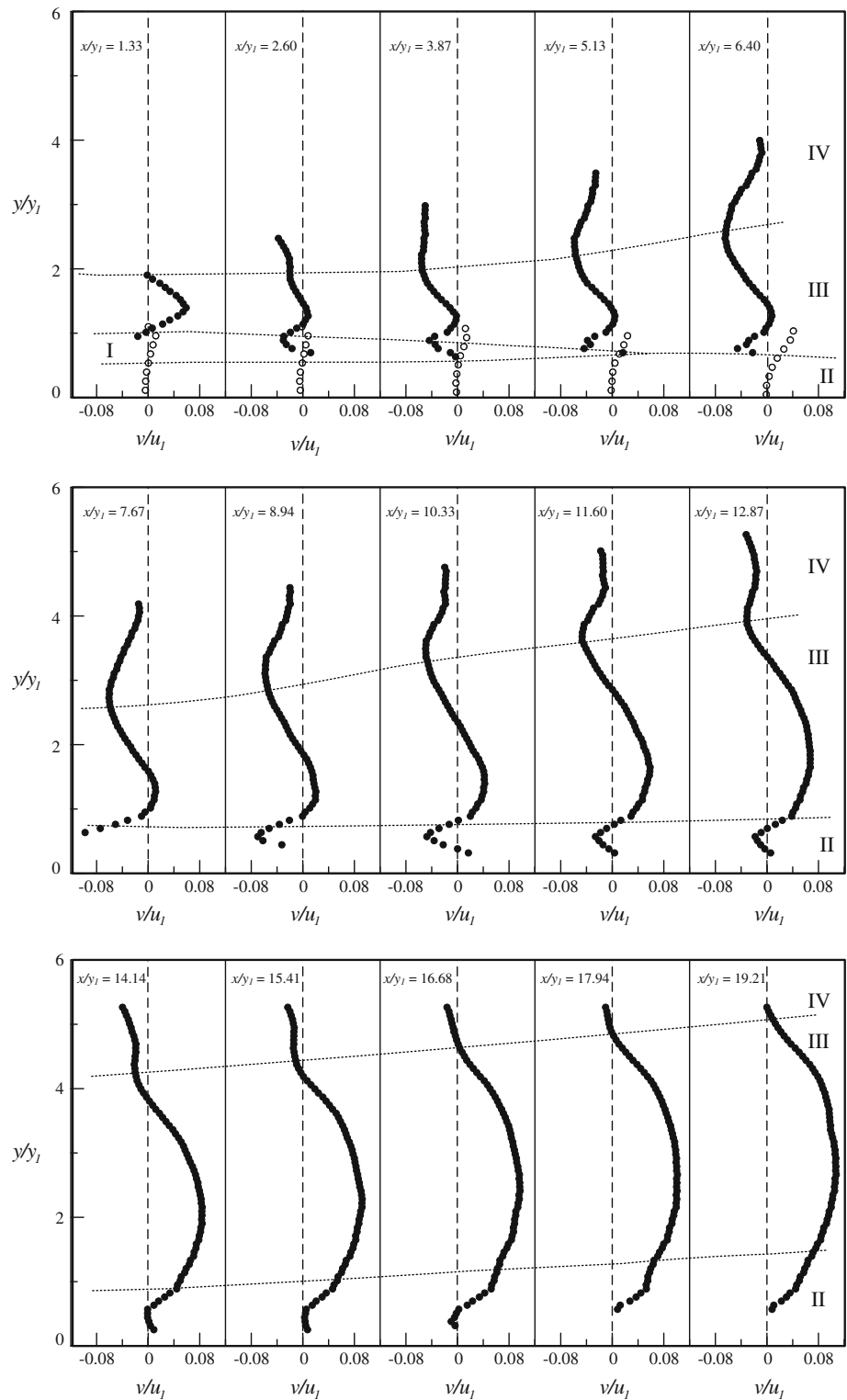


and observation in Chanson (2007), most bubbles are entrained at the toe of the jump and carried downstream by the flow. A certain number of bubbles are then rolled upstream by the reverse flow at the upper region of the roller and degassed. In the recirculation process, some

bubbles are carried downward to the overlap zone (i.e., the region with both valid PIV and BIV velocity measurements), intermittently, and ejected to the lower part of the jump. They therefore have a negative vertical velocity as observed in Fig. 10.



**Fig. 10** Vertical distributions of mean vertical velocity  $v/u_1$  at 15 cross-sections obtained by PIV and BIV for the  $F_r = 4.51$  jump corresponding to Fig. 9. *Open circle* water velocity by PIV measurements; *filled circle* bubble velocity by BIV measurements



The locations of maximum horizontal velocities for water and bubbles are nearly the same, and so as their variations. Figure 11 plots the ratio,  $r$ , of the maximum bubble velocities to the maximum water velocities with a nearly constant value of 0.66 for the  $F_r = 4.51$  jump.

Similar behavior was also observed in the other two different steady jump cases, except the ratio  $r$  depends on the Froude number ( $r = 0.73$  for the  $F_r = 5.00$  jump, and  $r = 0.76$  for the  $F_r = 5.35$  jump) and possibly also the physical dimensions of the jump (cannot be determined

from the present study). The value of  $r$  ranges from 0.6 to 0.8 for the present experiments. The slip velocity that may have a dominant effect on the value of  $r$  is a function of Reynolds number, bubble shape, bubble concentration, as well as several other flow properties (e.g., Zheng and Yapa 2000; Sathe et al. 2010) that are difficult to quantify in hydraulic jumps. Note that when bubbles are ejected into a uniform flow, the motion of bubbles and their velocities more or less follow that of water, as evidenced in Fig. 5e. When strong shear is present, bubbles no longer follow water. In such scenario, bubbles deform and rotate which in turn causes their motion to deviate from that of water and results in a lower mean bubble velocity.

It was observed that bubble entrainment in the steady jumps in the present study causes the flow to become very complicate and violent and renders the concentration of bubbles to become very high. It is not amenable to trace individual bubbles and compare their velocities with that of water. Alternatively, an experiment using a submerged jump was conducted to avoid the high air entrainment problem while retaining a similar shear flow as that of a surface steady jump. In the experiment, the water depths upstream and downstream of a sluice gate were 39.2 and 25.0 cm, respectively, and the opening of the sluice gate was 2.1 cm. The exit velocity of the submerged jet was 128.5 cm/s at the opening. A single CO<sub>2</sub> bubble was injected once at a time through a small stainless tube (located on the channel bed 10.0 cm upstream of the sluice gate) with an inner diameter of 1.6 mm. The same high-speed camera was used to record the bubble trajectory. PIV was also used to measure the mean water velocities of the single-phase submerged jump. The trajectories of some sample bubbles are plotted in Fig. 12 along with the mean water velocities. Note that in each trajectory plot, the snap shots of a single bubble with a time interval of 6.0 ms were superimposed. By comparing the bubble trajectory in the shear flow of the submerged jump to that in a uniform flow

(see Fig. 5), the bubbles in the submerged jump do not follow the water but mingled and twisted while moving downstream. Mean bubble velocities were calculated by averaging the instantaneous bubble velocities based on bubble locations and plotted on the top of mean water velocities of the submerged jump as shown in Fig. 13. The figure shows that the mean horizontal bubble velocities are lower than the mean horizontal water velocities, even though the bubbles have higher upward velocities due to buoyancy. The velocity ratio between the bubble velocity and the water velocity at each given location for the entire flow in the submerged jump is plotted in Fig. 14. An average ratio of 0.67 was found in the figure, consistent with the values of 0.6–0.8 found in the three steady surface jumps in the present study.

## 5 Turbulence statistics

Turbulence statistics of the jumps were also obtained through ensemble averaging the repeated PIV and BIV measurements. The results of the  $F_r = 4.51$  jump are plotted in Fig. 15, based on the bubble velocity measurements by BIV. The vertical distributions of non-dimensional root-mean-square (rms) horizontal and vertical bubble velocity fluctuations,  $U_{\text{rms}} = \sqrt{u'^2}/u_1$  and  $V_{\text{rms}} = \sqrt{v'^2}/u_1$ , are presented in Fig. 15a, b with  $u'$  being the horizontal bubble velocity fluctuations,  $v'$  being the vertical bubble velocity fluctuations, and the overbar denoting the ensemble-average operator. The non-dimensional in-plane equivalent turbulence intensity  $I = \sqrt{u'^2 + v'^2}/u_1$  and the non-dimensional equivalent Reynolds stresses  $\Lambda = -\overline{u'v'}/u_1^2$  are shown in Fig. 15c, d. The corresponding turbulence statistics for the weak jump has also been presented in Fig. 24 in “Appendix” for comparison.

The turbulence statistics at 10 vertical cross-sections taken from Fig. 15 are plotted in Fig. 16. Based on Fig. 16a,  $U_{\text{rms}}$  is very high in the potential core region for bubbles. The magnitude increases with respect to distance measured from the toe and reaches a maximum value of 0.89 at  $x/y_1 = 3.87$  and then decreases to a value of 0.53 toward the end of the potential core at  $x/y_1 = 5.13$ . This high magnitude seems to be unusual for a turbulence flow. The high fluctuations in the bubble velocities are likely due to that the bubbles in the potential core were intermittently injected from the mixing layer above. Each injection event corresponds to a high turbulent burst in the mixing layer; it in turn causes high turbulence fluctuations for bubbles in the potential core. This also explains the low velocity ratio ( $r$ ) between bubbles and water in the potential core. If the bubbles in such region were given enough time to develop, we believe they may eventually catch the water velocities

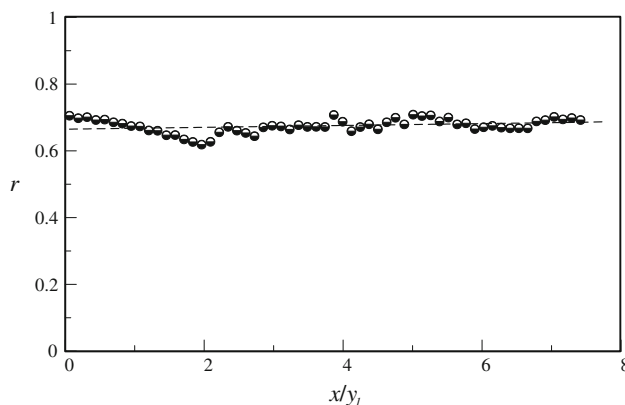


**Fig. 11** The corresponding ratio ( $r$ ) of maximum horizontal bubble velocity over maximum horizontal water velocity against  $x/y_1$



**Fig. 12** Sketch of the mean water velocity field of a submerged jump and randomly selected bubble trajectories in the jump. In each trajectory plot, the snap shots of a single bubble with a time interval of 6.0 ms were superimposed

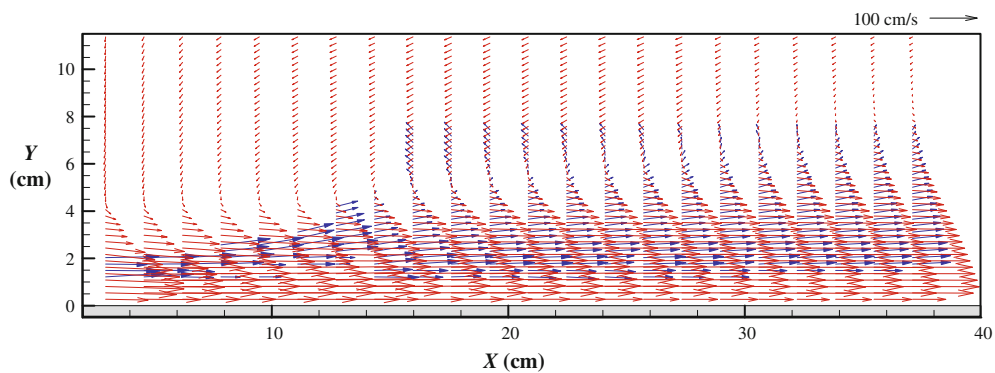
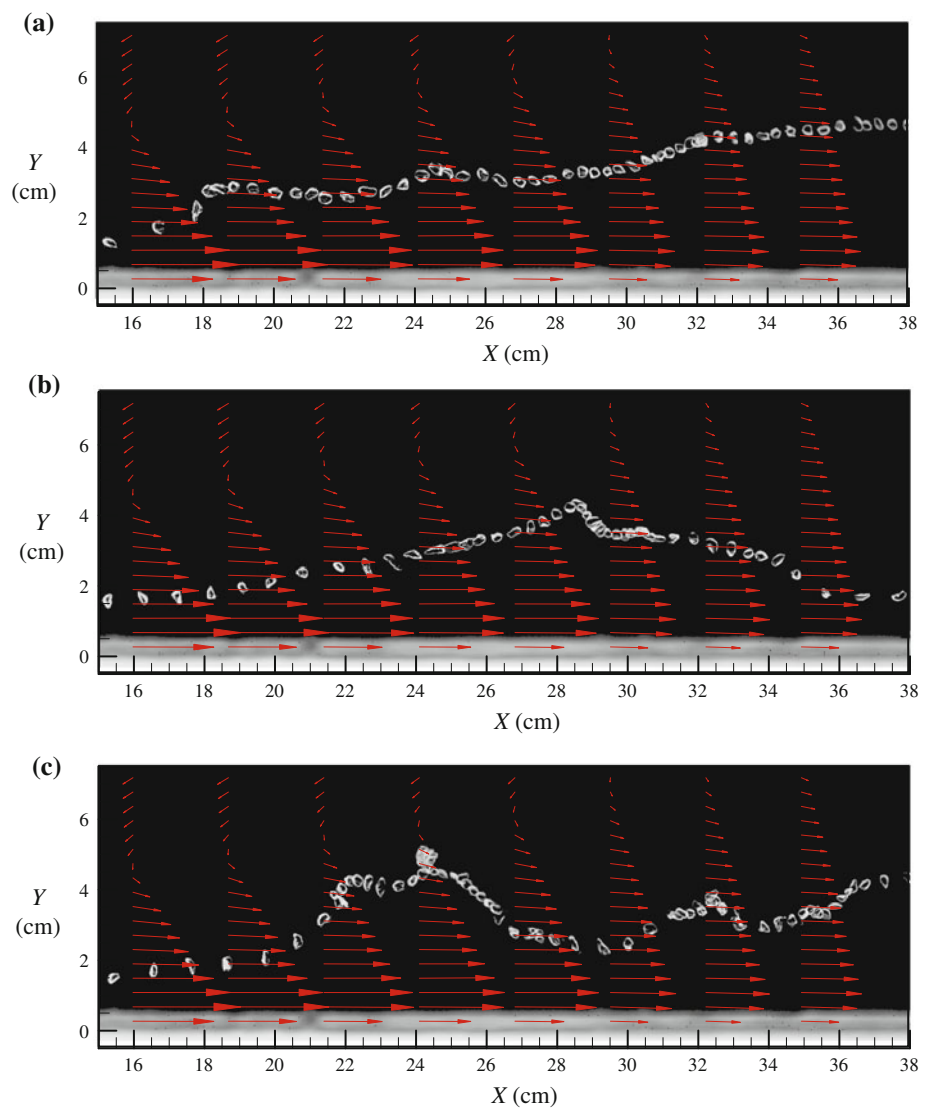


**Fig. 13** Superposition of mean bubble velocities (*blue*) measured from the bubble trajectories and mean water velocities (*red*) of the submerged jump

and result in an  $r$  value close to unity. In the boundary layer,  $U_{rms}$  is almost constant at about 0.4 for bubbles. In the mixing layer,  $U_{rms}$  decreases from 0.4 to 0.2 near the

upper bound of the mixing layer and then increases slightly in the recirculation zone. For water, the magnitude of  $U_{rms}$  is within a reasonable magnitude (about 0.2). The

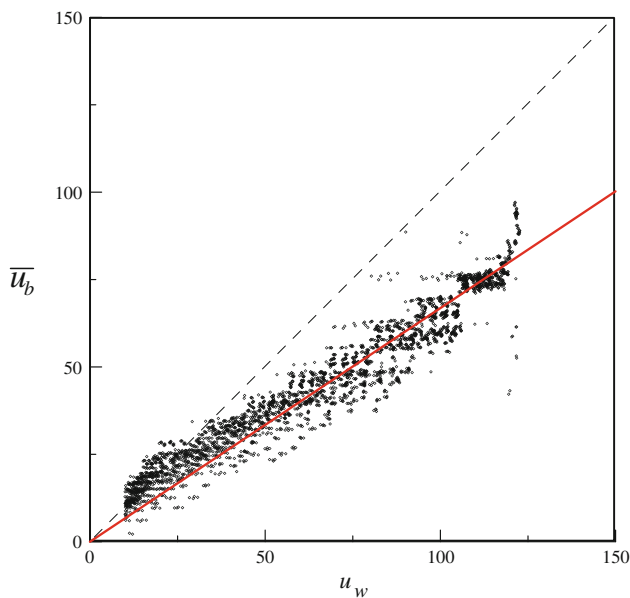


**Fig. 14** Mean horizontal bubble velocities measured from the bubble trajectories versus mean horizontal water velocities of the submerged jump. The *solid line* has a 0.67 slope

difference in  $U_{\text{rms}}$  between water and bubbles is huge in the overlap region. The cause of this huge difference is not clear, but could be attributed to the large velocity difference between water and bubbles (see Figs. 9, 10) with a low bubble concentration (based on video images) in such a region.

Figure 16b shows that the trend of  $V_{\text{rms}}$  is similar to that of  $U_{\text{rms}}$  except near the toe of the jump. Near the toe  $V_{\text{rms}}$  increases as the height  $y$  increases, though rather slowly, whereas  $U_{\text{rms}}$  decreases when  $y$  increases. Overall, the magnitude of  $U_{\text{rms}}$  is approximately twice that of  $V_{\text{rms}}$ . In the recirculation zone,  $U_{\text{rms}}$  and  $V_{\text{rms}}$  again follow the same trend and have a greater magnitude, corresponding to a higher entrainment of air bubbles. The non-dimensional in-plane equivalent turbulence intensity  $I = \sqrt{u'^2 + v'^2}/u_1$  is presented in Fig. 16c. Since the magnitude of  $U_{\text{rms}}$  is roughly twice that of  $V_{\text{rms}}$ , the value of  $I$  follows the same trend as that of  $U_{\text{rms}}$ . Even though velocities in the cross flume direction were not measured, we expect  $I$  to follow the same trend as well if that component was taken into account since there is no mean velocity gradient and forcing in that direction. The overall maximum of  $I$  is about 0.6, occurring near the lower bound of the mixing layer. Interestingly,  $I$  decreases in the mixing layer, even though the mean velocity gradient is the greatest in that region.  $I$  then increases slightly toward the free surface where the mean velocity gradient is

relatively small. The behavior seems to deviate from a typical mixing layer and contradicts with intuition. One should be aware that the turbulence statistics presented here are based on the bubble velocities, not water velocities.

The non-dimensional equivalent Reynolds stresses (or velocity covariance)  $\Lambda = -\overline{u'v'}/u_1^2$  for the bubble velocity fluctuations are illustrated in Fig. 16d. Near the toe of the jump ( $x/y_1 < 5.13$ ),  $\Lambda$  is positive. It then quickly decreases and becomes negative toward the free surface. Further downstream at  $x/y_1 > 6.4$ ,  $\Lambda$  is negative in the entire flow. The magnitude of  $\Lambda$  is higher near the free surface. Such a behavior is, although contradicting from intuition, consistent with the observation of  $I$ . The larger Reynolds stresses as well as higher turbulence intensity near the free surface may be due to a higher vertical velocities (see Fig. 10) caused by buoyant force as well as friction and drag among air bubbles in such a highest aeration region (all the bubbles must eventually come up to the free surface, also reported in Chanson 2011). The near-surface rollers and reverse flow beneath the free surface trap the bubbles that would otherwise move downstream. Along with the increase of water depth and lower horizontal velocities in the upper half of the jump (see Fig. 9), they are responsible for the relatively large values of  $\Lambda$  near the free surface. Furthermore, the magnitude of  $\Lambda$  decreases toward the downstream direction. Similar results were also observed by Liu et al. (2004) for hydraulic jumps with  $F_r = 2.0\text{--}3.2$ . Again, one should be aware that the turbulence statistics presented here are based on the bubble velocities, not water velocities; hence they may differ from those of water.

## 6 Similarity profile for horizontal bubble velocities

A nonlinear curve combining sine and exponential functions was employed to fit the mean horizontal bubble velocities in the mixing layer region in order to determine the appropriate length and velocity scales. The formula may be expressed as

$$u = C_0 \sin(C_1 y^{C_2} + C_3) \cdot \exp(-C_4 y)^2 + C_5 \quad (1)$$

where  $C_0$  to  $C_5$  are regression coefficients. Fitting curves obtained using Eq. (1) are shown as lines in Fig. 17 with  $R^2$  values of 0.99 for all the cross-sections when the constants were appropriately chosen using least square regression. This indicates that various velocity and length scales can be derived based on these curves.

Figure 18 depicts the detailed vertical distribution of mean horizontal bubble velocity  $u(y)$  for the  $F_r = 4.51$

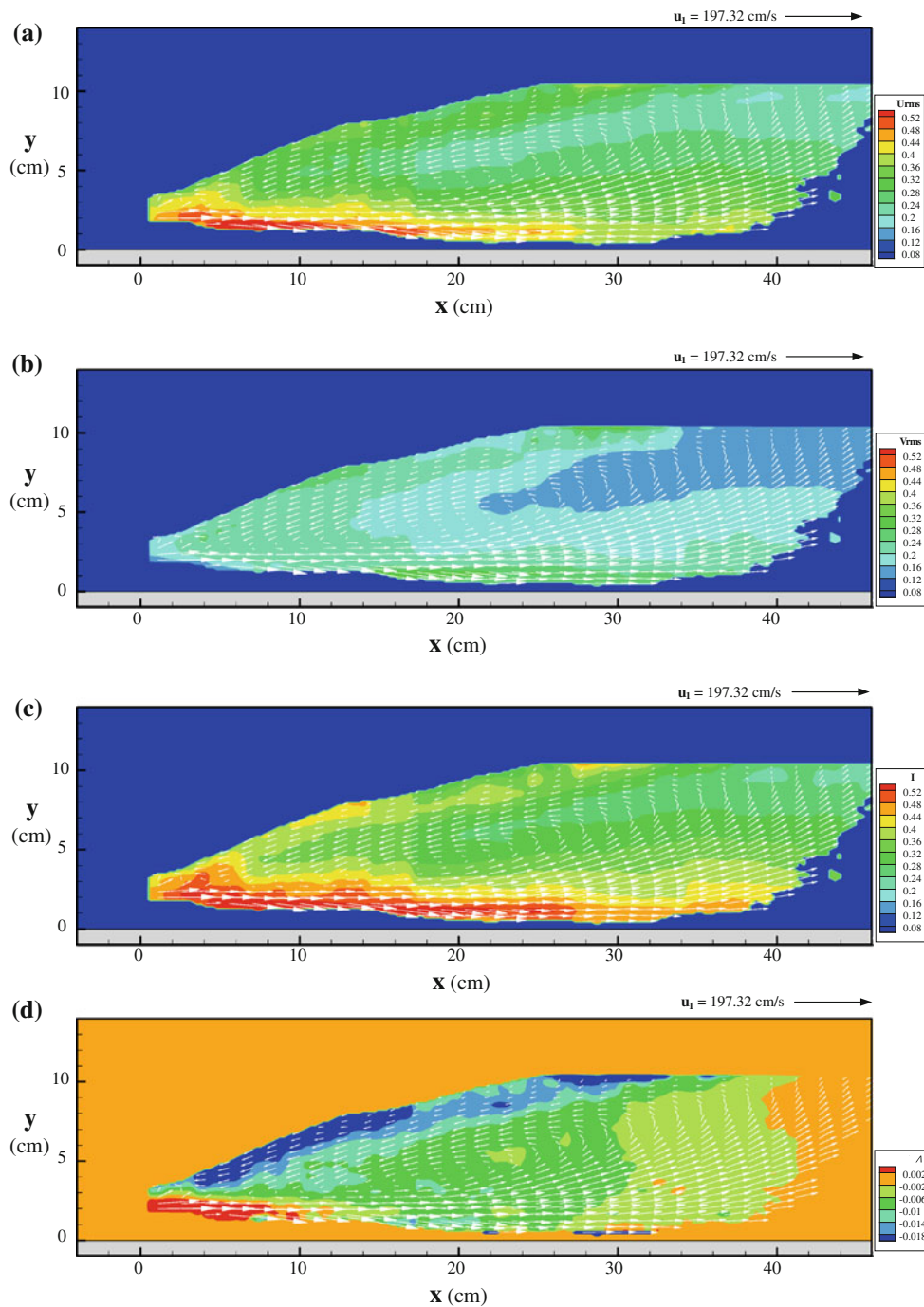


**Fig. 15** Non-dimensional turbulence statistics of the bubble velocities for the  $F_r = 4.51$  jump: **a**  $U_{rms} = \sqrt{u'^2}/u_1$ ; **b**  $V_{rms} = \sqrt{v'^2}/u_1$ ; **c** in-plane equivalent turbulence intensity  $I = \sqrt{u'^2 + v'^2}/u_1$ ; **d** equivalent Reynolds stresses  $\Lambda = -\overline{u'v'}/u_1^2$

jump at  $x/y_1 = 10.33$  (same as the middle panel in the middle row of Fig. 17 but in dimensional form). In the figure,  $u_{max}$  and  $u_{min}$  represent the maximum positive and maximum negative horizontal velocities with their positions at  $y_{umax}$  and  $y_{umin}$ , respectively. Based on different velocities examined for obtaining a similarity profile,

$(u_{max} - u_{min})$  was considered as the most appropriate velocity scale along with the typical length scale  $b$  being defined as the half-width of the mixing layer where  $(u_{max} - u_{min})/2$  occurs. Accordingly, the similarity profile was obtained by taking  $(u_{max} - u_{min})$  as the characteristic velocity scale and the representative mixing layer thickness

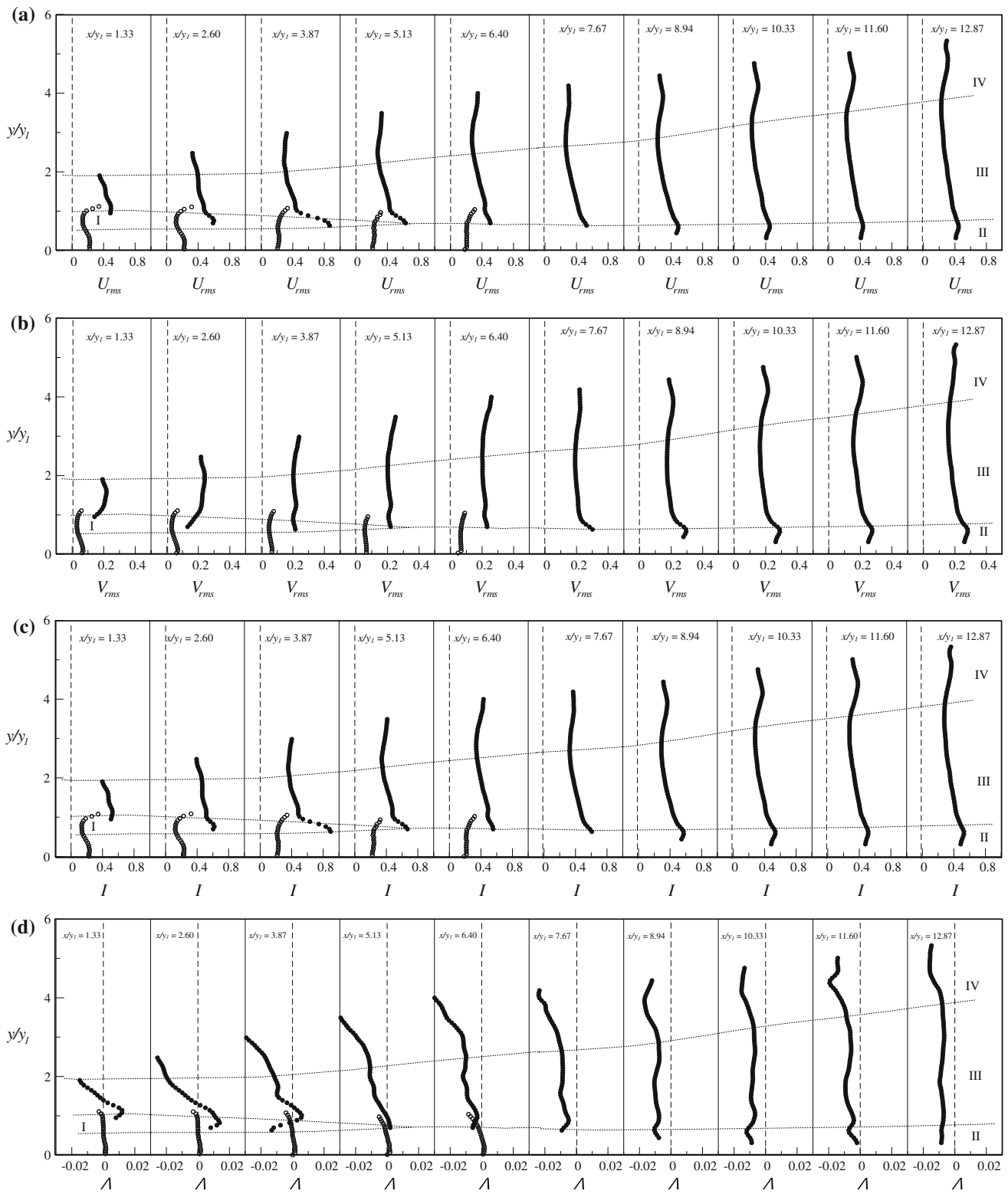
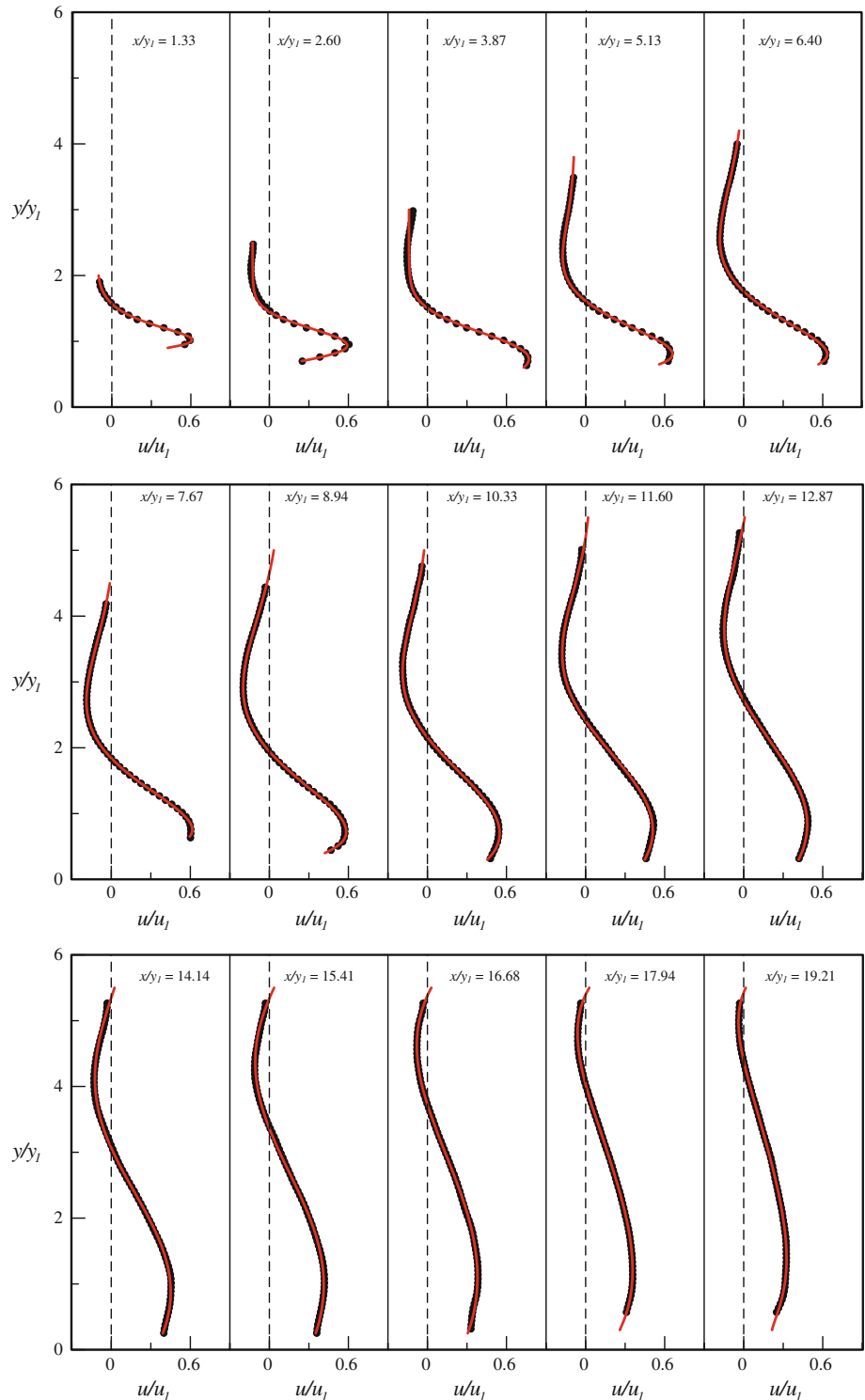


**Fig. 16** Non-dimensional turbulence statistics for the  $F_r = 4.51$  jump corresponding to Fig. 15: **a**  $U_{rms} = \sqrt{u^2}/u_1$ ; **b**  $V_{rms} = \sqrt{v^2}/u_1$ ; **c** in-plane equivalent turbulence intensity  $I = \sqrt{u^2 + v^2}/u_1$ ; **d** equivalent Reynolds stresses  $\Lambda = -\overline{uv^2}/u_1^2$ . Open circle water; filled circle bubbles

$(y_{u_{\min}} - y_{u_{\max}})$  as the characteristic length scale. The result for the dimensionless mean horizontal bubble velocity deficit  $(u - u_{\min})/(u_{\max} - u_{\min})$  versus the dimensionless shifted height  $(y - b)/(y_{u_{\min}} - y_{u_{\max}})$  is plotted in Fig. 19.

Note that the plot features cross-sections from the three different experimental cases (with  $F_r = 4.51, 5.00,$  and  $5.35$ ) based on the bubble velocities; they collapse onto a similarity profile expressed as:

**Fig. 17** Vertical distributions of mean horizontal bubble velocities with fitting curves for the  $F_r = 4.51$  jump



$$\frac{u - u_{\min}}{u_{\max} - u_{\min}} = 40.2 \times \sin \left[ 0.035 \left( \frac{y - b}{y_{u_{\min}} - y_{u_{\max}}} + 4.23 \right)^{3.30} - 1.95 \right] \times \exp \left[ -0.249 \left( \frac{y - b}{y_{u_{\min}} - y_{u_{\max}}} + 4.23 \right)^2 \right] + 0.117 \quad (2)$$

The  $R^2$  value is 0.99 in the fit. The figure shows that a promising similarity profile for the bubble velocities in the entire flow zone can be obtained except near the free surface in the recirculation region. In that near-surface region, the surface roller effect and violent surface fluctuations may be the cause of the scattering of experimental data from the similarity profile.

### 7 Wall-jet profile for water velocities

Rajaratnam (1965) conducted velocity measurements using a Pitot tube in a hydraulic jump and concluded that the velocity distribution in a hydraulic jump is similar to that in a typical wall jet. Based on the near-wall mean water velocities in the present study, experimental data from the three steady jump cases ( $F_r = 4.51, 5.00,$  and  $5.35$ ) as well as from the weak jump case ( $F_r = 2.43$ ) and data from Rajaratnam (1965) and Chanson and Brattberg (2000) were all plotted together and shown in Fig. 20. The vertical axis  $y$  and horizontal velocity  $u$  are normalized by the half-width of the wall jet  $b_w$  (based on the height where  $u_{\max}/2$  occurs) and the maximum horizontal velocity  $u_{\max}$ , respectively. Note that the PIV velocity measurements do not cover the region where the upper half-width occurs in the three high Froude number cases due to bubbles. An error function was used to fit the water velocity data to determine the location of the upper half-width since the velocity distribution of a wall jet can be described by the error function (Rajaratnam 1976). As shown in Fig. 20, the function indeed fits very well to the data (except the original data in Chanson and Brattberg are quite scattering), so using an error function for extrapolation fit may be appropriate. According to the velocity profile, the near-wall region of the hydraulic jumps does behave like a wall jet that can be expressed by an empirical equation as

$$\frac{u}{u_{\max}} = 2.3 \times \left( \frac{y}{b_w} \right)^{0.42} \times \left[ 1 - \operatorname{erf} \left( 0.886 \times \frac{y}{b_w} \right) \right] \quad (3)$$

where erf is the error function. The  $R^2$  value is 0.97 in the fit.

One may question that using a wall-jet velocity profile to fit the PIV velocity data for finding the upper half-width

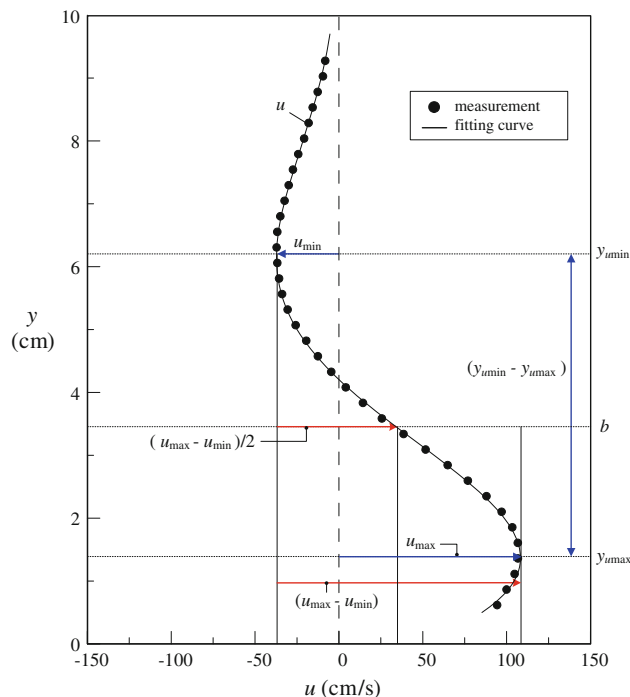


**Fig. 18** Vertical distribution of the mean horizontal bubble velocities with a fitting curve for the  $F_r = 4.51$  jump at  $x/y_1 = 10.33$  and definition of scales. Note that  $u_{\max} > 0$  and  $u_{\min} < 0$

for  $b_w$  may be somewhat questionable. For validation purpose, Chanson and Brattberg’s (2000) velocity measurements under a hydraulic jump were used. Since the data are rather scattering, they were not used in obtaining the empirical equation in Eq. (3). The similarity curve does go through the center of the cluster, indicating an appropriate prediction of wall-jet behavior. Indeed, if  $b_w$  is replaced by the location of the maximum horizontal water velocity  $y_{\max}$  (and therefore fitting an error function to find the upper half-width is no longer needed), a similarity profile of  $y/y_{\max}$  versus  $u/u_{\max}$  in the same functional form as that of Eq. (3) can also be found with data collapsing as good as that in Fig. 20 (not shown here).

### 8 Energy spectra and integral scales

The comparison of energy spectra and integral scales between water and bubbles and how they vary along a vertical cross section is shown in this section. Autocorrelation functions and energy spectra, and integral length scale in the overlap region (with both water and bubble velocities measured) at  $x = 15$  cm for the  $F_r = 5.0$  jump were calculated at every 0.25 cm. Results from two sample locations are shown in Fig. 21. According to the figure, the autocorrelation functions of water velocity fluctuations are wider, indicating a longer integral time scale. The energy



**Fig. 19** Similarity profile of the mean horizontal bubble velocities for all three steady jumps ( $F_r = 4.51, 5.00,$  and  $5.35$ )

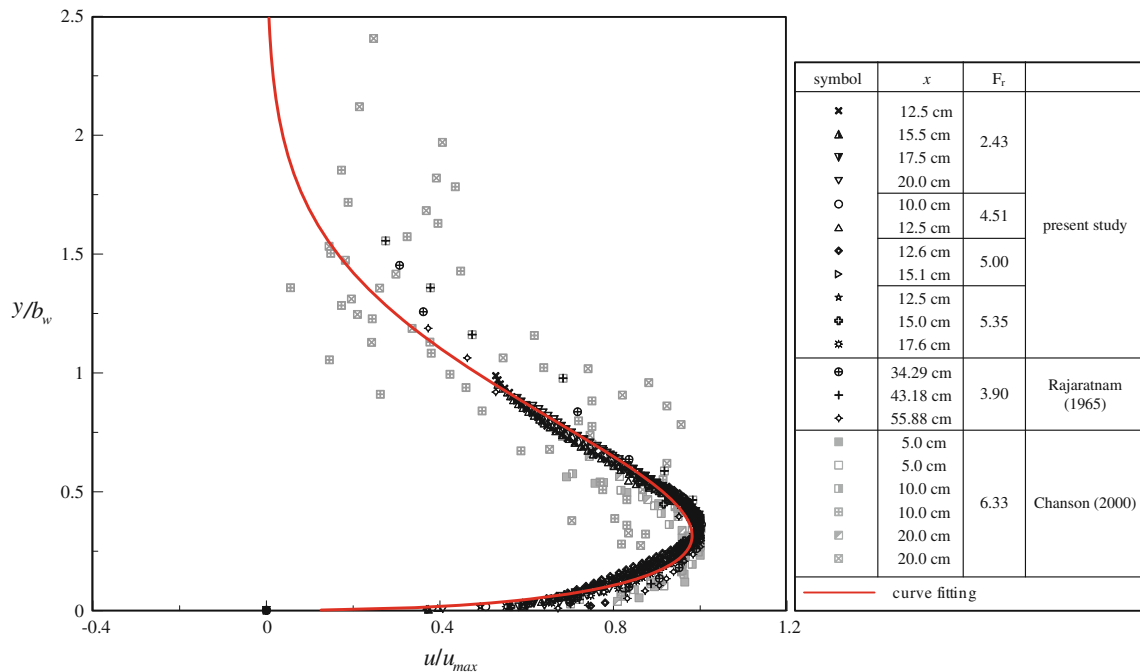
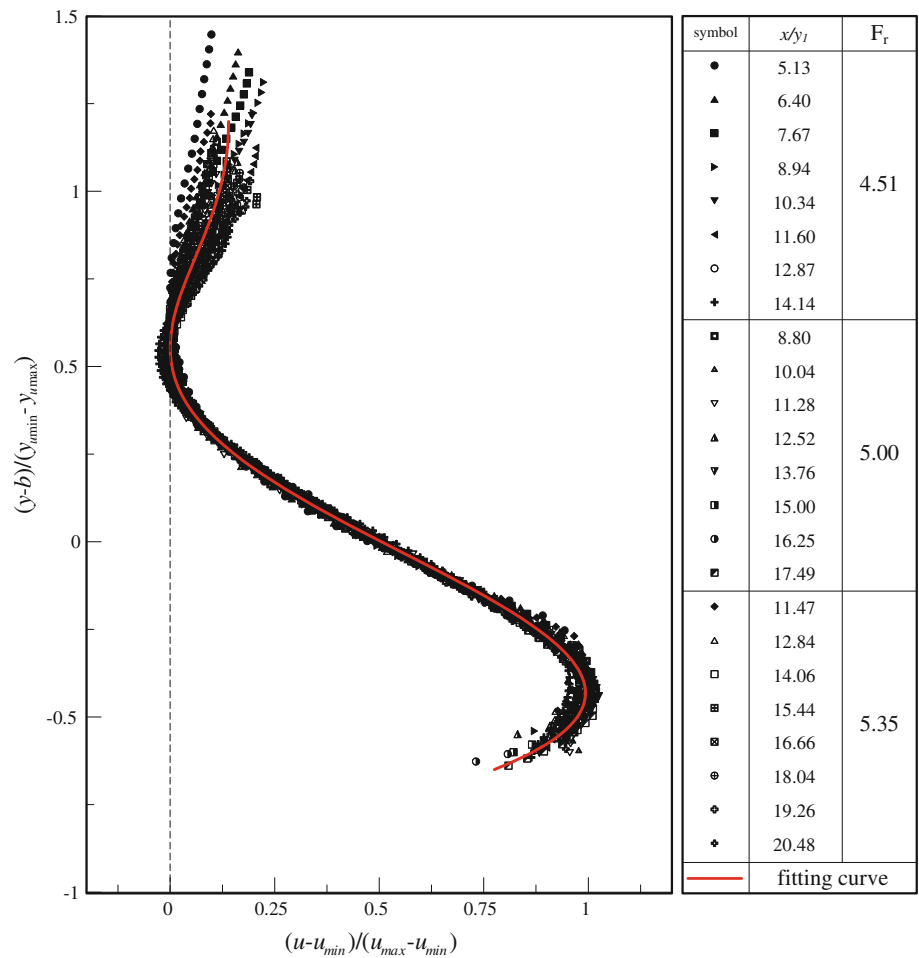
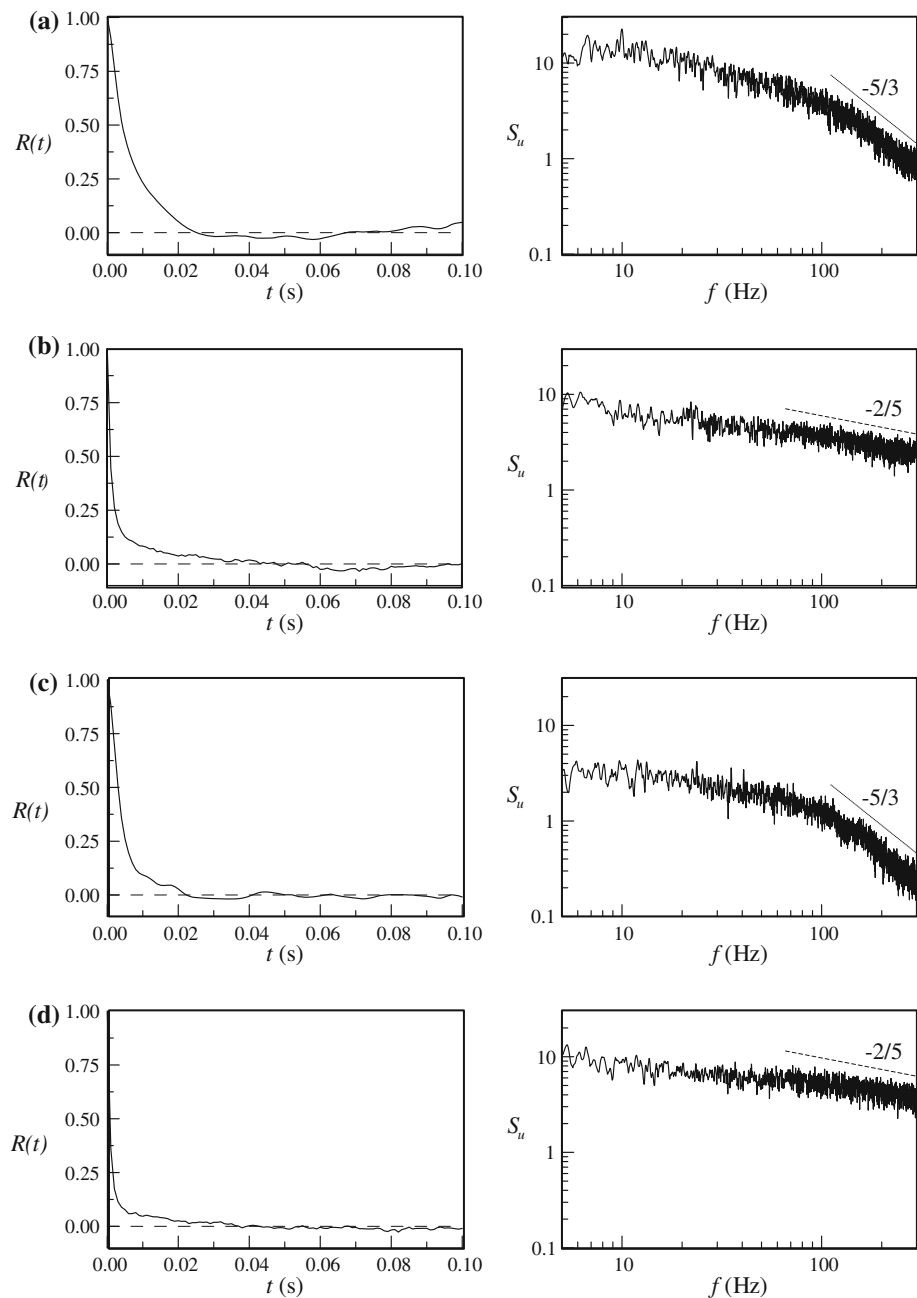


**Fig. 20** Wall-jet similarity profile of the mean horizontal water velocity in the near-wall region using data from the  $F_r = 2.43, 4.51, 5.00,$  and  $5.35$  jumps, and data in Rajaratnam (1965) and Chanson and Brattberg (2000)

**Fig. 21** Autocorrelation functions (*left panel*) and energy spectra (*right panel*) of the horizontal velocity fluctuations for  $F_r = 5.00$  jump at  $x = 15$  cm for **a** water at  $y = 1.5$  cm, **b** bubbles at  $y = 1.5$  cm, **c** water at  $y = 2.5$  cm, **d** bubbles at  $y = 2.5$  cm

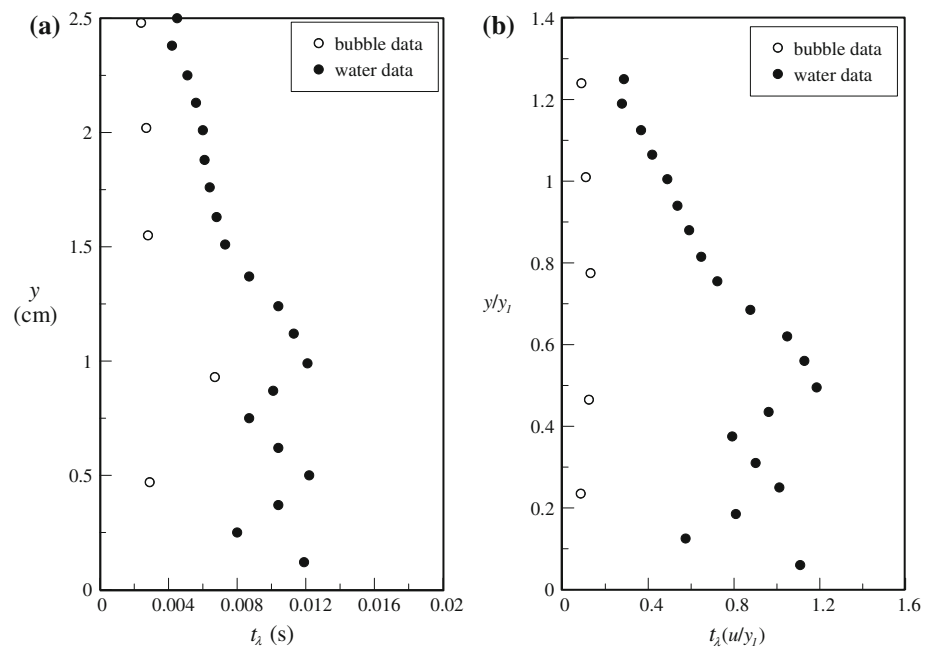


spectra of water velocity fluctuations follow the  $-5/3$  slope as expected, whereas the energy spectra of bubble velocity fluctuations are much flatter with a  $-2/5$  slope. Indeed, the  $-5/3$  slope for water was observed for the entire profile except very close to the bed, and the  $-2/5$  slope for bubbles was observed everywhere for the entire cross section. Note that in this overlap region, the occurrence of bubbles was intermittent rather than constantly present. The difference in the spectral slopes indicates that relatively higher turbulence was produced by bubbles at smaller scales, whereas turbulence production at large scales was

suppressed by bubbles. Similar phenomena were also reported in Shawkat et al. (2007) for bubbly pipe flows and in Bryant et al. (2009) for bubble plumes.

Figure 22a shows integral time scales ( $t_i$ ) for water and bubbles that were calculated by integrating the area beneath each autocorrelation function up to its first zero crossing. Since the mean velocities have been obtained (see Fig. 7), integral length scales ( $t_i u / y_1$ ) can be determined, as shown in Fig. 22b. It clearly shows that the length scale of water (about 1 for  $y/y_1 < 0.5$ ) is one order of magnitude greater than that of bubbles (about 0.1). Due to the

**Fig. 22** **a** Integral time scales and **b** integral length scales of the horizontal water and bubble velocities in the overlap region for the  $F_r = 5.00$  jump at  $x = 15$  cm



intermittency behavior in this overlap region, the length scale is alternating back and forth between these long and short scales in the jumps in the overlap region.

Indeed, the autocorrelation functions and energy spectra of bubble velocity fluctuations were also calculated at every 0.25 cm for the entire cross section at  $x = 15$  cm for the  $F_r = 5.0$  jump and three other cross-sections at  $x = 12.5, 30,$  and  $45$  cm. It was found that the energy spectral slope for bubbles is constant with the same  $-2/5$  slope for the entire depth for all four cross-sections (not shown here). Based on the autocorrelation functions at these four cross-sections and mean bubbles velocities, integral time scales and integral length scales were calculated and plotted in Fig. 23. The time scales increase as the distance from the toe of the jump increases. The two close cross-sections of  $x = 12.5$  and  $15$  cm are very close to each other and are for validation purpose to ensure the measurements and analysis are consistent (and the results show so). The time scales in Fig. 23a show a large increase (roughly doubled) at  $x = 45$  cm which is close to the constant depth region of the jump (see Fig. 7 for velocity field and surface profile), whereas the time scales are quite consistent among the  $x = 12.5, 15,$  and  $30$  cm cross-sections, especially above  $y = 3$  cm. Interestingly, the integral lengths in Fig. 23b show a consistent scale of about 0.2 near the free surface, even though the time scales of the  $x = 45$  cm cross section are much greater than the others. The length scales remain consistent among the  $x = 12.5, 15,$  and  $30$  cm cross-sections, and about 0.2 near the bed, whereas the length of the  $x = 45$  cm cross section deviates from the others more and more from the free surface and reaches 0.6 at the maximum near the bed. This may be due

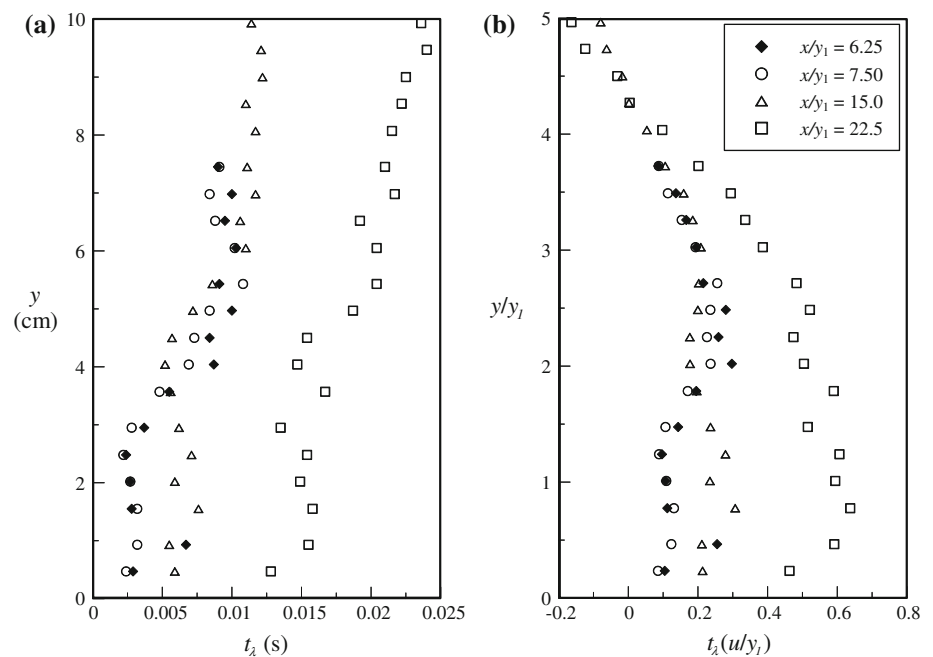
to the fact that the concentration of bubbles is lower in the lower part of  $x = 45$  cm cross section (there are no bubble velocities at the lower downstream part of the  $F_r = 4.51$  jump as shown in Fig. 7a due to a lack of bubbles).

## 9 Conclusions

The flow structure and turbulence statistics of three steady hydraulic jumps ( $F_r = 4.51$ – $5.35$ ) in both the non-aerated and aerated regions were measured using the image-based PIV and BIV techniques, respectively. The measurements were validated by measurements taken using LDV and tracking bubble trajectories in uniform flows and submerged jumps. A weak jump ( $F_r = 2.43$ ) was also measured to examine differences between a weak jump and a steady jump. Some findings are summarized as follows:

1. The BIV technique can be successfully employed to obtain detailed flow field in the aerated region of steady hydraulic jumps by correlating textures in the images formed by air bubbles. The technique was validated with velocities obtained from tracking the centroid of individual bubbles released into a uniform flow. The mean velocities of bubbles are the same with that of water if the flow is uniform. The bubble velocities are lower than the water velocities when shear is present, evidenced by observing individual bubbles released into a submerged jump.
2. The mean horizontal velocities measured using PIV in the water region and BIV in the aerated region in the potential core region are different but follow the same trend. The velocities of air bubbles are significantly

**Fig. 23** **a** Integral time scales and **b** integral length scales of the horizontal bubble velocities for the  $F_r = 5.00$  jump at  $x = 12.5$  cm (diamond), 15 cm (circle), 30 cm (triangle), and 45 cm (square)



lower than that of water; the air bubbles are subjected to drag forces in such a shear flow. However, the locations of the maximum horizontal velocities are coincident between water and bubbles. The ratio,  $r$ , of the maximum bubble velocity versus the maximum water velocity is nearly constant, and its magnitude depends on the Froude number and possibly the physical dimensions of the jump. In general,  $r$  varies between 0.6 and 0.8.

3. The flow structure of the steady jumps may be classified into the four regions based on the mean flow characteristics, namely the potential core, the boundary layer, the mixing layer, and the recirculation regions. However, all but the recirculation region were identified for the weak jump case. The potential core region follows the incoming supercritical flow that extends more than 10 approaching water depths beyond the toe of the steady jumps. The thickness of the bottom boundary layer increases gradually with the downstream distance, reaches the maximum value at the end of the potential core, and then onwards remains constant. The mixing layer, which is highly aerated, occurs right at the toe of the jumps and above the potential core with its thickness bounded by lines representing the maximum positive and maximum negative horizontal velocities. The recirculation region is above the mixing layer and near the free surface with the flow in the reverse direction and highly aerated.
4. The magnitude of the horizontal velocity fluctuations is approximately twice that of the vertical velocity fluctuations. The maximum level of equivalent turbulence intensity  $I$  based on the bubble velocity

fluctuations is about 0.6 which occurs near the lower bound of the mixing layer. However, in a small region of the potential core near the toe of the jump, the level reaches 0.89. The magnitude of  $I$  is lower in the mixing layer where the mean velocity gradient is relatively high and increases slightly toward the free surface where the mean velocity gradient is relatively low.

5. A unique similarity profile was found for mean horizontal bubble velocities by taking the representative mixing layer thickness as the characteristic length scale and the difference between the maximum positive and maximum negative bubble velocities as the characteristic velocity scale. The profile shows promising self-preservation in the aerated region.
6. A wall-jet similarity profile was validated for water velocities in the near-wall region. The profile is based on velocity data with Froude number ranging from 2.43 to 5.35 in the present study and data in Rajaratnam (1965) and Chanson and Brattberg (2000).
7. The slope of turbulence energy spectra follows the traditional  $-5/3$  slope for water. However, the slope was found to be  $-2/5$  for bubbles, regardless the location in the jumps, indicating a higher turbulence production by bubbles at smaller scales and a reduction of turbulence production at larger scales due to bubble suppression.

**Acknowledgments** The authors gratefully thank the financial support by the National Science Council of Taiwan under Grant Nos. NSC 99-2221-E-005-117-MY3 and NSC 100-2119-M-005-002, and by the Directorate General of the Highways Bureau, Ministry of Transportation and Communication of Taiwan.

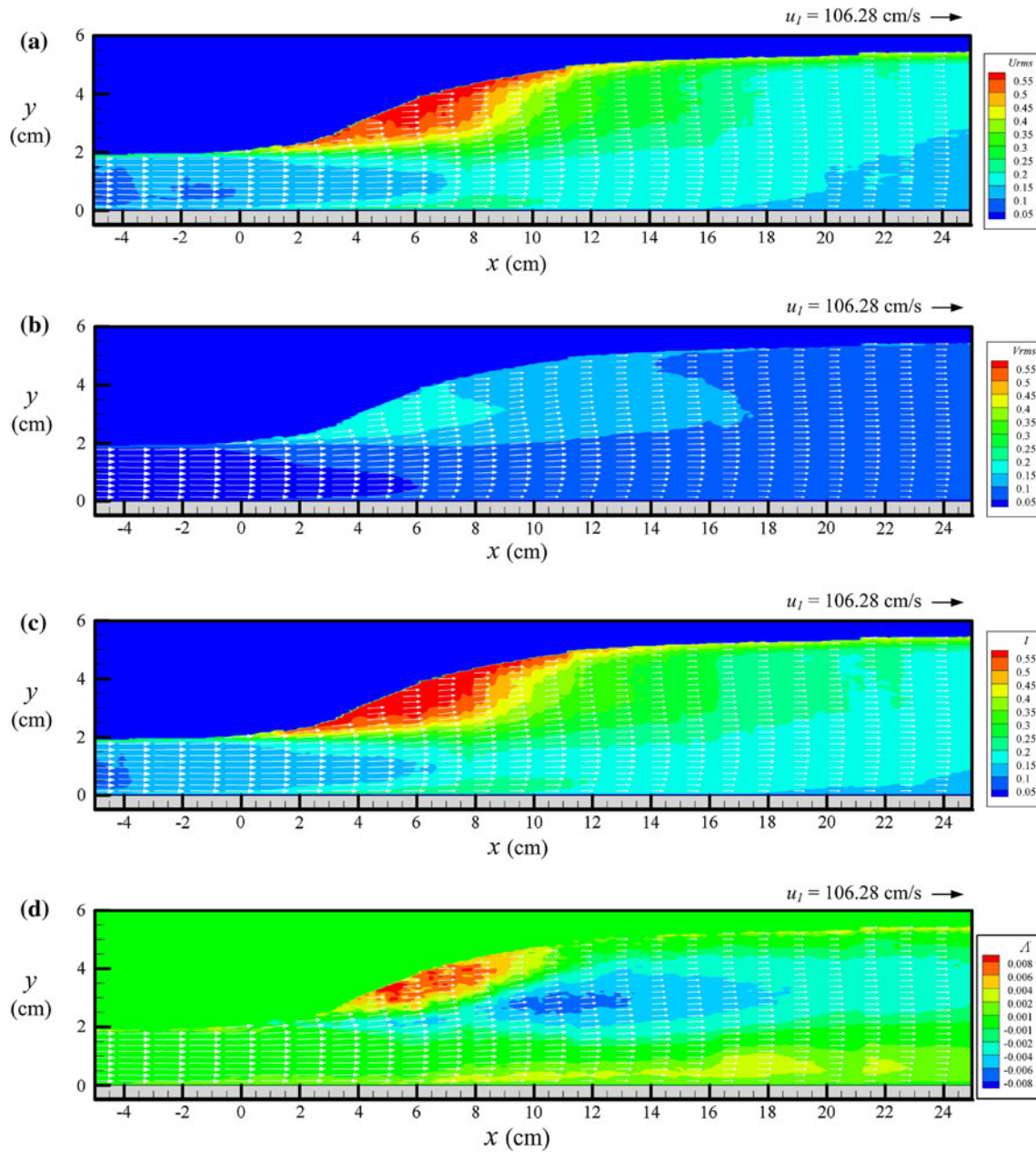


**Fig. 24** Turbulence statistics of the weak jump with  $F_r = 2.43$ . **a**  $U_{rms} = \sqrt{u'^2}/u_1$ ; **b**  $V_{rms} = \sqrt{v'^2}/u_1$ ; **c** in-plane turbulence intensity  $I = \sqrt{u'^2 + v'^2}/u_1$ ; **d** Reynolds stresses  $\Lambda = -\overline{u'v'}/u_1^2$

**Appendix: Turbulence statistics of weak jump with  $F_r = 2.43$**

In addition to the three steady hydraulic jumps ( $F_r = 4.51, 5.00, \text{ and } 5.35$ ) investigated in the present study, a weak jump with a Froude number of  $F_r = 2.43$  was also measured using the same techniques and analyzed using the same procedure. The turbulence statistics of the weak jump are plotted in Fig. 24. By comparing with the turbulence

statistics of steady jumps in Fig. 15, the high turbulence region in the weak jump overlaps with the region of high aeration (near free surface and behind the toe) as shown in Fig. 24. On the contrary, the high turbulence region occurs coincidentally with the maximum positive velocity region around the lower bound of the mixing layer in the steady jumps as shown in Fig. 15. The distributions of Reynolds stresses between the weak jump and the steady jumps are also very different.

## References

- Bakhtmeteff BA, Matzke AE (1935) The hydraulic jump in terms of dynamic similarity. *Trans Am Soc Civ Eng* 101:630–680
- Bryant DB, Seol DG, Socolofsky SA (2009) Quantification of turbulence properties in bubble plumes using vortex identification methods. *Phys Fluids* 21:075101
- Chang K-A, Lim H-J, Su CB (2003) Fiber optic reflectometer for velocity and fraction ratio measurements in multiphase flows. *Rev Sci Instrum* 74:3559–3565
- Chang K-A, Ariyaratne K, Mercier R (2011) Three-dimensional green water velocity on a model structure. *Exp Fluids*. doi: [10.1007/s00348-011-1051-0](https://doi.org/10.1007/s00348-011-1051-0)
- Chanson H (2007) Hydraulic jumps: bubbles and bores. In: *Proceedings of 16th Australasian fluid mechanic conference*, Gold Coast, Australia, pp 39–53
- Chanson H (2011) Bubbly two-phase flow in hydraulic jumps at large Froude numbers. *J Hydraul Eng* 137:451–460
- Chanson H, Brattberg T (2000) Experimental study of the air-water shear flow in a hydraulic jump. *Int J Multiph Flow* 26(4):583–607
- Chow VT (1973) *Open channel hydraulics*. The McGraw-Hill Book Co. Inc., Singapore
- Hager WH (1992) *Energy dissipators and hydraulic jump*. Kluwer, The Netherlands
- Hornung HG, Willert C, Turner S (1995) The flow field downstream of a hydraulic jump. *J Fluid Mech* 287:299–316
- Hoyt JW, Sellin RHJ (1989) Hydraulic jump as mixing layer. *J Hydraul Eng* 115(12):1607–1614
- Keane RD, Adrian RJ (1992) Theory of cross-correlation analysis of PIV images. *Appl Sci Res* 49:191–215
- Lennon JM, Hill DF (2006) Particle image velocity measurements of undular and hydraulic jumps. *J Hydraul Eng* 132(12):1283–1294
- Leutheusser HJ, Kartha VC (1972) Effects of inflow condition on hydraulic jump. *J Hydraul Div Am Soc Civ Eng* 98(8):1367–1384
- Lin C, Hwung WY, Hsieh SC, Chang KA (2007) Experimental study on mean velocity characteristics of flow over vertical drop. *J Hydraul Res* 45(1):33–42
- Lin C, Hsieh SC, Kuo KJ, Chang KA (2008) Periodic oscillation caused by a uniform flow over a vertical drop energy dissipater. *J Hydraul Eng* 134:948–960
- Liu M, Rajaratnam N, Zhu D (2004) Turbulence structure of hydraulic jumps of low Froude numbers. *J Hydraul Eng* 130(6):511–520
- Long D, Steffler P, Rajaratnam N (1990) LDA study of flow structure in submerged hydraulic jump. *J Hydraul Res* 28(4):437–460
- Long DJ, Rajaratnam N, Steffler PM, Smy PR (1991) Structure of flow in hydraulic jumps. *J Hydraul Res* 29(2):207–218
- Mehrotra SC (1976) Length of hydraulic jump. *J Hydraul Div Am Soc Civ Eng* 102(7):1027–1033
- Misra SK, Kirby JT, Brocchini M, Veron F, Thomas M, Kambhamettu C (2008) The mean and turbulent flow structure of a weak hydraulic jump. *Phys Fluids* 20:035106
- Mossa M, Tolve U (1998) Flow visualization in bubbly two-phase hydraulic jump. *J Fluid Eng* 120:160–165
- Murzyn F, Mouaze D, Chaplin JR (2005) Optical fibre probe measurements of bubbly flow in hydraulic jumps. *Int J Multiph Flow* 31:141–154
- Rajaratnam N (1965) The hydraulic jump as a wall jet. *J Hydraul Div Am Soc Civ Eng* 91(5):107–132
- Rajaratnam N (1976) *Turbulent jets*. Elsevier, Amsterdam, pp 216–218
- Rajaratnam N, Subramanya K (1968) Profile of the hydraulic jump. *J Hydraul Div Am Soc Civ Eng* 94(3):663–673
- Resch FJ, Leutheusser HJ, Alemu S (1974) Bubbly two-phase flow in hydraulic jump. *J Hydraul Div Am Soc Civ Eng* 100(1):137–149
- Rouse H, Ince S (1957) *History of hydraulics*. Iowa Institute of Hydraulic Research, University of Iowa, Iowa City, IA
- Rouse H, Siao TT, Nagarathnam S (1958) Turbulence characteristics of the hydraulic jump. *J Hydraul Div Am Soc Civ Eng* 84(1):1–30
- Ryu Y, Chang KA (2008) Green water void fraction due to breaking wave impinging and overtopping. *Exp Fluids* 45:883–898
- Ryu Y, Chang KA, Lim HJ (2005) Use of bubble image velocimetry for measurement of plunging wave impinging on structure and associated greenwater. *Measu Sci Tech* 16:1945–1953
- Ryu Y, Chang KA, Mercier R (2007) Runup and green water velocities due to breaking wave impinging and overtopping. *Exp Fluids* 43:555–567
- Sathe MJ, Thaker IH, Strand TE, Joshi JB (2010) Advanced PIV/LIF and shadowgraphy system to visualize flow structure in two-phase bubbly flows. *Exp Fluids* 65:2431–2442
- Shawkat ME, Ching CY, Shoukri M (2007) On the liquid turbulence energy spectra in two-phase bubbly flow in a large diameter vertical pipe. *Int J Multiph Flow* 33:300–316
- Svendsen I, Veeramony J, Bakunin J, Kirby J (2000) The flow in weak turbulent hydraulic jumps. *J Fluid Mech* 418:25–57
- Zheng L, Yapa PD (2000) Buoyant velocity of spherical and nonspherical bubbles/droplets. *J Hydraul Eng* 126:852–854